One-Dimensional Time-Dependent Modeling of GATE Cumulonimbus Convection

BRAD SCHOENBERG FERRIER AND ROBERT A. HOUZE, JR.

Department of Atmospheric Sciences, University of Washington, Seattle, Washington

(Manuscript received 11 April 1988, in final form 25 July 1988)

ABSTRACT

A one-dimensional time-dependent cumulonimbus model is designed that, unlike in previous one-dimensional models, simulates cloud-top heights, vertical velocities, and water contents that are reasonably consistent with those observed in real convective cores. The model successfully simulates deep tropical oceanic cumulonimbus with results that are in agreement with aircraft observations of vertical velocity, observations of radar reflectivity, and three-dimensional model simulations. These results are achieved by improving the parameterizations of the following physical processes: vertical mixing through the inclusion of an overturning thermal circulation near cloud top, lateral entrainment by modifying the assumed shape of the cloud, initiating convection with sustained boundary-layer forcing that resembles the lifting by gust fronts associated with tropical oceanic cumulonimbus, and making the pressure perturbation internally consistent with the horizontal distribution of vertical velocity in the cloud. The effect of a tilted updraft on precipitation fallout and enhanced cloud growth are also examined.

1. Introduction

In the past, one-dimensional cloud models have been criticized for exhibiting internal inconsistencies when tested against observations. Warner (1970) noted that certain one-dimensional steady-state Lagrangian models were unable to predict correct values of cloud-top height and liquid water content simultaneously in simulations of shallow, nonprecipitating cumuli. Cotton (1975) confirmed this result and also found that one-dimensional time-dependent (1DTD) Eulerian models exhibited a similar deficiency in simulations of the initial growing stages of a convective cloud. Using a three-dimensional cloud model, Cotton and Tripoli (1978) showed that clouds simulated with no mean wind behaved like the 1DTD model clouds, whereas incorporating vertical shear of the horizontal wind produced clouds that possessed cloud water contents and vertical velocities that agreed more closely with observations. These findings have since discouraged many investigators from using one-dimensional models to study the dynamics of cumulus clouds.

Despite these shortcomings, the relative simplicity and economy of one-dimensional cloud models still make them attractive for various purposes. For example, parameterizations of ice-phase microphysical processes in cloud models can be applied and tested more economically and efficiently in a one-dimensional model. In addition, one-dimensional cumulus models have been used to compute the gross effects of ensembles of convective clouds on the larger-scale environment (e.g., Yanai et al. 1973; Ogura and Cho 1973; Arakawa and Schubert 1974; Kreitzberg and Perkey 1977; Anthes 1977; Nitta 1977; Johnson 1978, 1980; Brown 1979; Fritsch and Chappell 1980; Houze et al. 1980; Pointin 1985; Frank and Cohen 1987). Recently, Adler and Negri (1988) used a one-dimensional cumulus model to infer convective cloud intensity from infrared satellite data (see also Wylie 1979; Griffith et al. 1981; Adler and Mack 1984, 1986). Srivastava (1985, 1987) used a one-dimensional, time-dependent model of convective-scale downdrafts to determine their intensity as a function of the thermodynamic instability of the environment, and the cooling associated with the evaporation of raindrops and melting of ice particles. In the past, one-dimensional models have also been used to diagnose the efficiency of cloud seeding experiments (e.g., Simpson and Wiggert 1969). These examples of the utility of one-dimensional cloud models, together with the fact that three-dimensional cloud models remain computationally cumbersome and expensive for studies that require many model simulations, illustrate the continuing desirability to obtain a one-dimensional cumulus model that is internally consistent and captures the essence of cloud structure.

Besides the general desirability for a useful and physically reasonable one-dimensional cloud model, we are motivated to obtain such a model for a specific purpose. In the past several years, observational studies of squall lines with trailing stratiform precipitation regions have been conducted for tropical squall lines (Houze 1977; Zipser 1977; Gamache and Houze 1982,

Corresponding author address: Dr. Brad S. Ferrier, Severe Storms Branch, NASA/Goddard Space Flight Center, Greenbelt, Maryland 20771.

1983, 1985; Houze and Rappaport 1984; Roux et al. 1984; Roux 1985; Chong et al. 1987) and midlatitude squall lines (Ogura and Liou 1980; Smull and Houze 1985, 1987a,b; Srivastava et al. 1986). Based upon these observational studies, the following conceptual model has evolved. In these squall-line systems, ordinary (nonsupercellular), short-lived convective cells are initiated by the forced lifting of low-level ambient air by gust fronts at the front of the storm (Houze and Betts 1981; LeMone et al. 1984; Nicholls 1987; Dudhia et al. 1987). These cells move rearward as they mature and eventually become incorporated into the region of trailing stratiform precipitation upon their dissipation. The storm-relative winds also carry hydrometeors and high moist static energy air detrained from the convective cells rearward into the stratiform region at middle and upper levels. Thus, the deep convective cells in the line act as sources of heat and condensate for the stratiform zone. Rutledge and Houze (1987) have calculated the water budget and microphysical processes in a stratiform region in which ice particles are advected across an upstream boundary separating the convective and stratiform regions. These calculations are sensitive to the vertical distributions of hydrometeors above the 0°C level that are assumed to flow across the boundary from the convective region, and little information exists regarding what these profiles should be. The ultimate aim of this study is to diagnose the typical vertical distributions of hydrometeors in squall-line convective cells. From such diagnoses, together with knowledge of the relative airflow across the line, the flow of hydrometeors from the mid-to-upper reaches of the convective cells into the trailing stratiform region can be determined.

Further details of the conceptual model and the application of the 1DTD model for the study of tropical and midlatitude squall-line systems will be part of a future study. Since the 1DTD model cannot explicitly resolve the effects of environmental wind shear on the structure of the simulated convection, results from this study will be presented in the form of hypotheses to be verified in future studies using more sophisticated numerical models. It should also be noted that this conceptual model is not applicable for the study of midlatitude squall lines that consist of three-dimensional, quasi-steady supercells (Rotunno et al. 1988).

The objective of this paper is to design an improved 1DTD cumulus model that would be suitable for such preliminary diagnostic studies of ordinary, short-lived squall-line convection. The result is a model that has largely eliminated the internal inconsistencies among cloud height, vertical velocity, and water contents that plagued previous 1DTD models. Because of the availability of extensive datasets obtained in the Global Atmospheric Research Program's Atlantic Tropical Experiment (GATE), we have tested the model by simulating deep oceanic tropical convection typical of the GATE region in the eastern tropical Atlantic. For deep GATE convection, the new model simultaneously predicts vertical velocities and radar reflectivities (which are closely related to water content) that are consistent with GATE aircraft observations of in-cloud vertical velocities (LeMone and Zipser 1980; Zipser and LeMone 1980) and GATE radar data (Warner and Austin 1978; Szoke and Zipser 1986; Szoke et al. 1986). The new model results are also consistent with three-dimensional model simulations of GATE cumulonimbus (Simpson and van Helvoirt 1980; Simpson et al. 1982, 1986).

This internally consistent model has been achieved by redesigning the parameterizations of vertical and horizontal mixing, precipitation fallout, perturbation pressure, and methods of model initialization. Key features of the new model are 1) an overturning thermal circulation parameterized at the top of the cloud, which produces more reasonable vertical mixing and vertical distributions of perturbation pressure, 2) a modified cloud shape that leads to more reasonable rates of lateral entrainment, 3) a revised diagnostic pressure perturbation equation that is consistent with the distribution of vertical velocity in the cloud, 4) sustained low-level forcing that mimics the lifting of boundary-layer air by gust fronts observed during GATE (Frank 1978; Frank et al. 1981; Houze and Betts 1981; Addis et al. 1984), and 5) accounting for the effects of environmental wind shear only by parameterizing the fallout of precipitation from tilted convective updrafts. These innovations are described in sections 2 and 3, where the focus will be on the dynamical formulation of the model. Section 4 briefly describes the sensitivity runs that were made to test how changes in the parameterized physics of the model affected the simulated cloud growth. The model is tested by comparing its results with GATE data and with three-dimensional model output in section 5. Conclusions are presented in section 6.

2. Description of the model

The model is formulated in a cylindrical coordinate system (r, λ, z) following Ogura and Takahashi (1971). All dependent variables ( ) are defined as deviations from their environmental $(\ )_e$ values, while any quantity with $(\ )_c$ represents the actual value of a quantity within the cloud, expressed as

$$(\ )_c = (\ )_e + (\ ). \tag{1}$$

The model predicts cloud-averaged values of vertical velocity ($\bar{w}$ in m s^{-1}), potential temperature ($\bar{\theta}$ in degrees K), water vapor mixing ratio ($\overline{q_v}$ in g kg^{-1}), cloud water mixing ratio ($\overline{q_{cw}}$ in g kg^{-1}), rainwater mixing ratio ($\overline{q_r}$ in g kg^{-1}), and pressure perturbation relative to the large-scale environment.

a. Area-averaged equations

If A represents the value of any of the quantities w, θ, q_v, q_{cw}, or q_r, then the horizontal average of A over the area of a cloud of radius R is given by

$$\bar{A} = \frac{1}{\pi R^2}\int_0^{2\pi}\int_0^R Ardrd\lambda. \tag{2}$$

An average along the outer boundary of the cloud is

$$\tilde{A} = \frac{1}{2\pi}\int_0^{2\pi} A(R)d\lambda, \tag{3}$$

where $A(R)$ is the value of A at $r = R$. Deviations of A from $\bar{A}$ and $\tilde{A}$ are given by A' and A'', respectively. Unless otherwise stated, axial symmetry and no tangential winds are assumed in the model.

The anelastic form of the mass continuity equation is

$$\frac{1}{r}\frac{\partial(ru)}{\partial r} + \frac{1}{\rho_e}\frac{\partial(\rho_e w)}{\partial z} = 0, \tag{4}$$

where ρ_e is the density of the environment, assumed to be a function of height only, and u is the radial velocity, dr/dt. The area-averaged form of the mass continuity equation, given by

$$\frac{2}{R}\left(\tilde{u} - \tilde{w}\frac{\partial R}{\partial z}\right) + \frac{1}{\rho_e R^2}\frac{\partial}{\partial z}(\rho_e R^2\bar{w}) = 0, \tag{5}$$

is a result of applying (2) to (4), using Leibnitz' rule of integration (Hildebrand 1976, p. 365) and taking into account changes in cloud radius with height.

The prognostic equation for an arbitrary variable A in cylindrical coordinates is

$$\frac{dA_c}{dt} = \frac{\partial A_c}{\partial t} + \frac{1}{r}\frac{\partial(ruA_c)}{\partial r} + \frac{1}{\rho_e}\frac{\partial(\rho_e wA_c)}{\partial z}. \tag{6}$$

By averaging (6) over the cell's horizontal area, making use of (1) and (5), neglecting small changes with time in the properties of the large-scale environment, and assuming that

$$\tilde{A}_c = \begin{cases} \bar{A}_c, & \partial(\rho_e R^2\bar{w})/\partial z < 0 \\ A_e, & \partial(\rho_e R^2\bar{w})/\partial z > 0 \end{cases}, \tag{7}$$

we obtain

$$\frac{\partial\bar{A}}{\partial t} = -\frac{\partial A_e}{\partial t} - \bar{w}\frac{\partial A_e}{\partial z} + \frac{\overline{dA_c}}{dt} \quad \text{(i)}$$

$$+ \frac{\tilde{A}}{\rho_e R^2}\frac{\partial}{\partial z}(\rho_e R^2\bar{w}) \quad \text{(ii)} \qquad - \frac{1}{\rho_e R^2}\frac{\partial(\rho_e R^2\overline{wA})}{\partial z} \quad \text{(iii)}$$

$$- \frac{2}{R}\left(\widetilde{u''A''} - \widetilde{w''A''}\frac{\partial R}{\partial z}\right). \quad \text{(iv)} \tag{8}$$

To satisfy mass continuity, it is assumed in (7) that environmental air is entrained into the convective core if the cell-averaged vertical mass flux ($\rho_e\pi R^2 w$) increases with height, whereas air from the convective cell is detrained into the environment if the cell-averaged vertical mass flux decreases with height.

Term (i) in (8) represents the sources and sinks of the dependent variable $\bar{A}$; it takes on the following forms in the equations for vertical momentum, the thermodynamic energy, and mixing ratios of water vapor, cloud water, and rain:

$$\frac{\overline{dw}}{dt} = \bar{B} - R_d\theta_{ve}\frac{\partial\bar{P}}{\partial z}, \tag{9}$$

$$\frac{\overline{d\theta}}{dt} = \frac{L}{\tau C_p}(\text{PCOND} + \text{PREVP}), \tag{10}$$

$$\frac{\overline{dq_v}}{dt} = -\text{PCOND} - \text{PREVP}, \tag{11}$$

$$\frac{\overline{dq_{cw}}}{dt} = \text{PCOND} - \text{PRAUT} - \text{PRACW}, \tag{12}$$

$$\frac{\overline{dq_r}}{dt} = \text{PREVP} + \text{PRAUT} + \text{PRACW} + \overline{\frac{1}{\rho_e}\frac{\partial}{\partial z}(\rho_e\hat{V}_r q_r)}, \tag{13}$$

where

$$\bar{B} = g\left(\frac{\bar{\theta}}{\theta_e} + 0.61\overline{q_v} - \overline{q_L}\right),$$

$$\tau = \left(\frac{p_c}{1000}\right)^{R_d/C_p}, \tag{14}$$

P is the nondimensional pressure

$$\bar{P} = \frac{T_{ve}\bar{p}}{\theta_{ve}p_e}, \tag{15}$$

and T_{ve} and θ_{ve} are the virtual temperature and the virtual potential temperature of the environment. The last term in (14) represents the reduction of cloud buoyancy by "water loading" with $\overline{q_L} = \overline{q_{cw}} + \overline{q_r}$. The terms PCOND, PRAUT, PRACW, and PREVP represent the rates of net condensation (or evaporation) of cloud water, autoconversion of cloud water into rain, collection of cloud water by rain, and evaporation of rain, respectively. A brief description of these warm-rain microphysical processes is given in appendix A. The last term in (13) is the vertical flux convergence of rain, where $\hat{V}_r$ is the mass-weighted fallspeed associated with a population of raindrops (see section 2f).

b. Horizontal entrainment

In (8), there are two contributions to the net entrainment of air into convective cells from their sides:

term (ii) represents the horizontal inflow of air needed to satisfy mean mass continuity, known as "dynamic entrainment"; term (iv), referred to as "lateral eddy mixing," represents the turbulent mixing of air from the immediate environment into the convective cores without the net exchange of mass across cell boundaries. It is crucial that both processes of horizontal entrainment be resolved accurately since they strongly affect cell growth and internal properties. Note that the asymmetric component of dynamic entrainment associated with cumulus-scale vortices is not considered in the current parameterization (Tripoli and Cotton 1980; Simpson et al. 1982, 1986).

The terms "cells" and "cores" will be used synonymously in the following discussion to denote convective elements possessing significant vertical motion (i.e., updrafts and downdrafts) during their phase of most active development.

1) DYNAMIC ENTRAINMENT

Dynamic entrainment in a 1DTD model is determined by the assumed shape of the convective core's volume and the vertical profile of vertical velocity. Traditionally, a 1DTD convective cell is assumed to be a cylinder of fixed radius around a vertical axis, with little attention paid to the effect this arbitrary assumption of cell shape has on model performance. We allow for the possibility of different shapes of convective cores by letting the cell radius vary with height (Fig. 1). Given the same vertical profile of $\bar{w}$ increasing with height, the dynamic entrainment of air from outside the convective core is significantly reduced if the radius of the core is assumed to decrease with height (Fig. 1b) rather than remaining constant with height (Fig. 1a). Thorough testing of the 1DTD model suggests that it is impossible to simulate deep tropical convection with a constant cell radius unless unrealistically large forcing is applied to the model. By allowing the radius of the cell to decrease with height, the dilution of the convective cell through dynamic entrainment is reduced enough to permit deep convection to form under much more realistic conditions.

The vertical distribution of cell radius $R(z)$ used in the model assumes that the mass flux below some height Z_R is conserved for an idealized profile of vertical velocity, $\hat{w}(z)$;

$$R(z) = \begin{cases} R_0\left[\dfrac{\rho_e(0)\hat{w}(0)}{\rho_e(z)\hat{w}(z)}\right]^{1/2}, & z \leq Z_R \\ R(Z_R), & z > Z_R \end{cases} \quad (16)$$

$$\hat{w}(z) = w_0 + w_1\left(\frac{z}{Z_R}\right) \quad \text{for} \quad z \leq Z_R. \quad (17)$$

For values of $w_0 = 1$ m s^{-1}, $w_1 = 1.75$ m s^{-1}, $Z_R = 4$ km, and $R_0 = 1$ km, the radius R of the convective cell decreases nonlinearly with height from $R = 1$ km at the surface to $R = 0.73$ km for $z = 4$ km. During the early stages of cell growth when the convective core is dominated by active updraft, this profile of cell radius, which is shown in Fig. 1b, closely resembles LeMone and Zipser's (1980) aircraft analysis for the ten percent strongest updraft cores observed during GATE. Model simulations are also made using a constant radius profile with $R(z) = R_0$ for all heights.

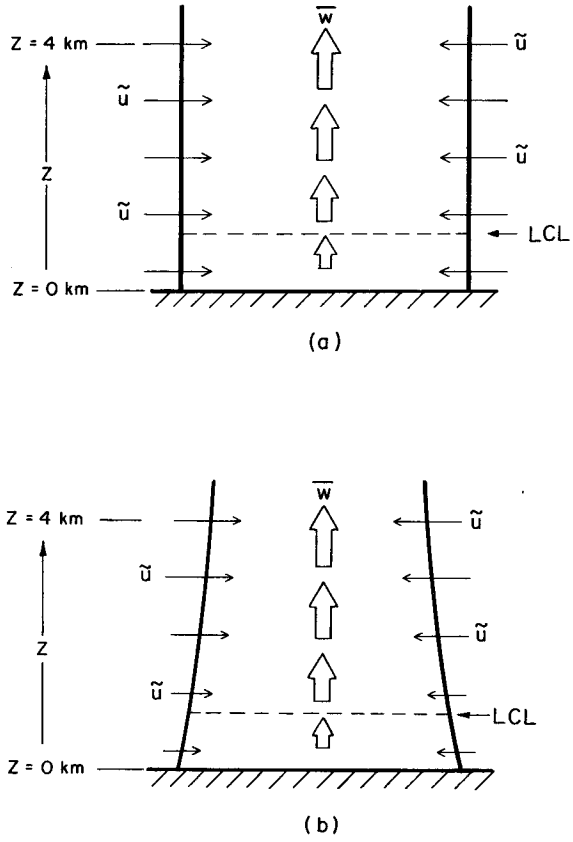

FIG. 1. A schematic depicting how the dynamic entrainment, represented by the horizontal flow across the cloud boundaries, is affected by the vertical profile of cloud radius. If the vertical distribution of $\bar{w}$ is the same for both cases, then the dynamic entrainment of environmental air above cloud base is stronger in (a), where the radius is constant with height, than in (b), which has the cloud radius decreasing with height.

The dilution of in-core properties by dynamic entrainment is also affected by the value assumed for A_e in (7). According to (7), the air transported across the cell's lateral boundaries from outside the convective cell is assumed to have the same thermodynamic properties as the large-scale environment. However, this is likely to be incorrect. Deep convection during GATE was almost never isolated, but instead tended to develop within areas of apparent saturation on the mesoscale (Houze and Betts 1981; Tao and Simpson 1984). The thermodynamic structure within such a region may differ significantly from the large-scale environment represented by radiosonde measurements.

The range of responses in the 1DTD model to possible assumptions about the properties of the entrained air are investigated in section 5.

2) LATERAL EDDY MIXING

Observational evidence suggests that the entrainment by turbulent mixing along the sides of the clouds [term (iv) in (8)] is much smaller than the entrainment that occurs near cloud top (Warner 1969; Paluch 1979; LaMontagne and Telford 1983; Boatman and Auer 1983; Austin et al. 1985; Jensen et al. 1985). In the 1DTD model, the lateral eddy mixing should therefore proceed at a much slower rate than the vertical eddy mixing. Thus, we decided that neglecting the process of lateral eddy mixing would serve as an interesting and useful parameterization. Such a formulation is also consistent with the parameterization of lateral entrainment derived by Randall and Huffman (1982). Unless otherwise indicated, the model calculations make this assumption. In a few simulations, the sensitivity of the model to lateral eddy mixing was tested using Asai and Kasahara's (1967) parameterization, which has been used in most previous 1DTD models. They assume that

$$\widetilde{u''A''} - \widetilde{w''A''}\frac{\partial R}{\partial z} = \alpha^2|\bar{w}|\bar{A}, \tag{18}$$

with α assumed to be 0.1.

c. *Vertical fluxes*

The vertical flux wA may be written as

$$\overline{wA} = \bar{w}\bar{A} + \overline{w'A'}. \tag{19}$$

One of the major problems in 1DTD cloud modeling has been to represent adequately the contribution of the eddy term in (19) to the vertical transport represented by term (iii) in (8). In previous studies it has been ignored (Asai and Kasahara 1967; Ogura and Takahashi 1971; Holton 1973; Yau 1979), represented using relatively simple eddy-viscosity schemes that assume only down-gradient, diffusive-type mixing (Cotton 1975; Ryan and Lalousis 1979), or parameterized in terms of the turbulence intensity within the cell (Lopez 1973; Pointin 1985).

A parameterization of vertical eddy mixing was developed based on data gathered in instrumented aircraft flights through tropical convective cores (LeMone and Zipser 1980; Zipser and LeMone 1980; Warner et al. 1980; Jorgensen et al. 1985) and midlatitude updraft cores (McCarthy 1974; Sand 1976; Kyle et al. 1976; Hallett et al. 1978). These data indicate that most in-cloud quantities possess systematic horizontal variations at larger scales across active convective cells and smaller, random turbulent fluctuations. This evidence is corroborated by simulations using two- and three-dimensional cloud models (e.g., Murray 1970; Murray and Koenig 1972; Schlesinger 1978a; Simpson and van Helvoirt 1980; Simpson et al. 1982). Excluding turbulent fluctuations, values of most quantities tend to change monotonically from some value at the center of the convective cell to values close to that of the large-scale environment near the edge of the cell.

Accordingly, it is assumed that the dependent variables in the model can be described as follows:

$$w = w_r(r) + w^* \tag{20}$$

$$A = A_r(r) + A^*, \tag{21}$$

where $w_r(r)$ and $A_r(r)$ are the systematic radial distributions assumed for w (vertical velocity) and the arbitrary variable A, while w^* and A^* represent the small-scale, turbulent fluctuations of w and A with respect to the assumed distributions $w_r(r)$ and $A_r(r)$. Simple linear functions are used to represent $w_r(r)$ and $A_r(r)$:

$$w_r(r) = w_0(1 - xr/R) \tag{22}$$

$$A_r(r) = A_0(1 - yr/R), \tag{23}$$

where w_0 and A_0 are the values of w and A at the center of the convective core, and x and y are dimensionless constants that control how much w and A change between the center and edge of the core. For example, the "top-hat" profile is assumed when $x = y = 0$ (used in previous 1DTD models). But if $x = y = 1$, then $w_r(r)$ and $A_r(r)$ change from w_0 and A_0 at the center of the convective cell to zero (the environmental values) along the cell boundary at $r = R$. This triangular-shaped distribution is typical of the vertical velocity profiles measured in aircraft flights through GATE convective cores (LeMone and Zipser 1980; Zipser and LeMone 1980) and in convective cells embedded in hurricanes (Jorgensen et al. 1985).

By applying (2) to (20)–(23), we obtain

$$w_0 = 3\bar{w}/(3 - 2x) \tag{24}$$

$$A_0 = 3\bar{A}/(3 - 2y). \tag{25}$$

These expressions relate the peak values of w and A to their in-cloud averages. A singularity occurs when $x = 1.5$ and $y = 1.5$ in (24) and (25) because the area average of such a distribution is zero regardless of the value of that quantity at the center of the convective core—i.e., the contribution made to the horizontal area average at $r < 2R/3$ is completely balanced by an equal and opposite contribution at $r > 2R/3$. If x and y are greater than 1.5, then w and A are of opposite sign to w_0 and A_0. Such a distribution is clearly unlike what has been observed in real cumulonimbus clouds. If the values of x and y are less than zero, then $w(R) > w_0$ and $A(R) > A_0$, which is also contrary to what has been simulated in multidimensional cloud models and observed in real convective cores during periods of active growth. We assert that $0 < x, y < 1.2$ is generally consistent with aircraft data and two- and three-dimensional model simulations.

Our method for estimating the area-averaged vertical fluxes within convective cells is based on the above representations of w and A. By taking the area average of the product wA after substituting for w and A using (20) and (21),

$$\overline{wA} = \overline{w_r(r)A_r(r)} + \overline{w^*A^*} + \overline{w_r(r)A^*} + \overline{w^*A_r(r)},$$

in which the last two terms on the right side of the equation are neglected since the small-scale turbulent fluctuations are assumed to be random and of much smaller scale than the convective core. Using (22)–(25) and taking the area average of $w_r(r)A_r(r)$, the area-averaged vertical flux of A is

$$\overline{wA} = \chi_A \bar{w}\bar{A} + \overline{w^*A^*} \tag{26}$$

with

$$\chi_A = \frac{3(3xy - 4x - 4y + 6)}{2(3 - 2x)(3 - 2y)}. \tag{27}$$

An expression for the vertical eddy flux of A is found by combining (19) and (26), giving

$$\overline{w'A'} = (\chi_A - 1)\bar{w}\bar{A} + \overline{w^*A^*}. \tag{28}$$

This equation decomposes the eddy flux into two components. The first term on the right is the contribution of the assumed systematic triangular shape of the basic cross-cell profiles of w and A to the eddy correlation, while the second term on the right is the vertical eddy flux contributed by smaller-scale eddies randomly superimposed on the triangular structure.

d. Vertical mixing

Numerous studies suggest that entrainment into cumulus clouds is strongest near cloud top (e.g., Squires 1958; Warner 1969, 1970; Paluch 1979; Telford and Wagner 1981; LaMontagne and Telford 1983; Boatman and Auer 1983; and others). It has also been shown that tropical convection typically possesses a bubble- or thermal-like structure near cloud top. These cloud-top thermals are regions of enhanced convective overturning, where warm, buoyant ascent in the middle of the convective element is surrounded by a narrow region of descent along the periphery of the element (e.g., see review articles by Simpson 1983a,b,c). A vertical eddy mixing scheme is formulated that links both sets of observations. First, the contribution to the vertical eddy flux of A by the largest scale of motion (the triangular variation across the cell), represented by the first term on the right side of (28), is specified to represent an overturning, thermal-like circulation near the top of the convective core. The vertical derivative of this eddy flux term gives the vertical eddy mixing of A due to the cloud-top thermal circulation. Second, the vertical derivative of $\overline{w^*A^*}$, the vertical eddy flux of A contributed by the small-scale turbulent eddies, results in the subgrid-scale vertical mixing of A. The parameterizations for both scales of vertical mixing are outlined in the following subsections.

1) A THERMAL-LIKE CIRCULATION PARAMETERIZED NEAR CLOUD TOP

Studies using multilevel aircraft data as early as the mid-1950s have shown that an overturning thermal-like circulation commonly exists near the tops of actively growing tropical cumuli (e.g., Scorer and Ludlam 1953; Malkus 1954; Malkus and Scorer 1955) that strongly resembles the thermals produced in laboratory experiments (Scorer and Ronne 1956; Scorer 1957; Woodward 1959; Saunders 1962). Simulations of tropical convection using two-dimensional axisymmetric models (e.g., Murray 1970, 1971; Murray and Koenig 1972; Soong and Ogura 1973, 1976; Libersky 1980) and three-dimensional models (Yau 1980; Simpson and van Helvoirt 1980; Turpeinen and Yau 1981; Simpson et al. 1982) have also reproduced thermal-like, vortical circulations at cloud top during the active stages of growth.

The model assumes that a thermal- or bubble-like circulation exists near the tops of actively growing cumulus clouds, where, with guidance from all of the studies cited above, a relatively simple conceptual model determines what the values as a function of height and time are of the parameters x and y that determine the triangular profiles of w and A.

To simulate the effects of a thermal circulation at cloud top, the model cell is divided with respect to height into four distinct regions, depicted in Fig. 2 as regions R_1 through R_4 for the case of a cylindrical convective core. Regions R_2 and R_3 represent the so-called

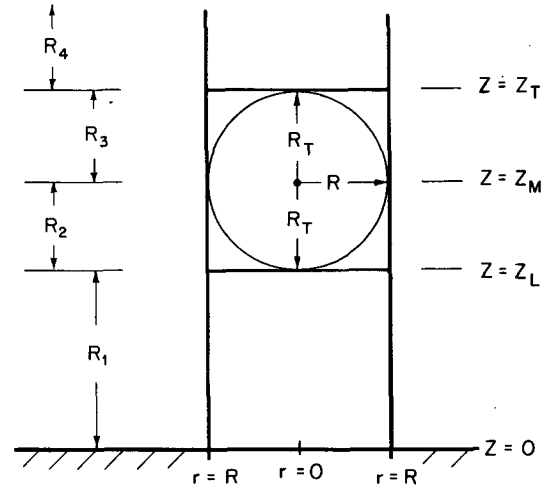

FIG. 2. The various regions in the model cloud that are defined with respect to the cloud-top height (Z_T). Regions R_2 and R_3 comprise the thermal cap region, R_1 is the lower region of the convective cell, and R_4 is the environment above cloud top. The vertical depth of the thermal cap region is $2R_T$, where it is assumed that $R_T = R_0 = R$ ($z = 0$) throughout the model run.

"thermal-cap region." The top of this thermal cap region is defined with respect to the cloud top height Z_T (defined by the $\overline{q_L} = 0.1$ g kg^{-1} isoline). The region of environmental air above cloud top is represented by R_4, while R_1 contains the lower portion of the convective cell extending from the surface up to the base of the thermal cap at $z = Z_L$.

Figure 3 shows how the horizontal distribution of vertical velocity is parameterized in the model. Setting $x = 1$ and having triangular-shaped profiles of vertical velocity in region R_1, descent is parameterized along the cell's periphery near cloud top by increasing the value of x with height in regions R_2 and R_3. The model configuration resembles that of Turner's (1962) starting plume, where the convective element has the characteristics of a jet at low levels capped by a thermal circulation at cloud top.

The desired thermal is produced by prescribing the x coefficient in (23) as

$$x(t, z) = \begin{cases} x^L, & z \leqslant z_L \\ x^L + (x^M - x^L)\left(\dfrac{z - z_L}{R_T}\right), & z_L < z < z_M \\ x^M + (x^T - x^M)\left(\dfrac{z - z_M}{R_T}\right), & z_M < z < z_T \\ x^T, & z \geqslant z_T, \end{cases} \tag{29}$$

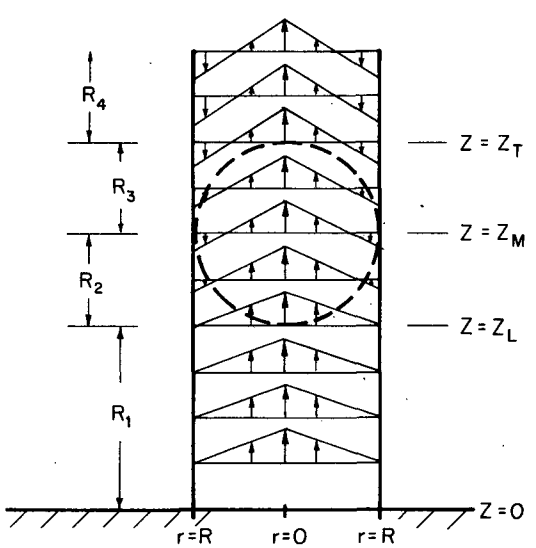

FIG. 3. A diagram showing how the thermal circulation is parameterized in the thermal cap region, where the horizontal distributions of $w_r(r)$ are given as a function of height and each profile is normalized to give a constant value of w_0. Note that the triangularity x in the updraft profiles increases with height only in the thermal cap region. Thus, for $x = 1$ at $z \geqslant Z_L$ and increasing with height in R_2 and R_3 to $x = 1.5$ at $z = Z_T$, an overturning circulation is approximated just below cloud top.

TABLE 1. Coefficients used in thermal cap region.

Variable	Coefficients	Values of coefficients $z = Z_L$	$z = Z_M$	$z = Z_T$
w	x	1.0	1.1	1.2
θ	y_θ	0.75	1.0	1.1
q_v	y_v	0.75	0.9	1.0
q_{cw}	q_{cw}	0.75	0.9	1.0
q_r	q_r	0.75	0.9	1.0

where X^L is the value of x assumed in R_1, X^M is the value of x in the center of the thermal at $z = Z_M$, X^T is defined at and above the cloud-top height Z_T, and $R_T = R_0$ is the vertical depth of the thermal. Equations analogous to (29) are used to describe $y(t, z)$ in (23). In Table 1, the values for x, y_θ, y_v, y_{cw}, and y_r at levels Z_L, Z_M, and Z_T are used to determine the vertical profiles of x and y in the parameterized thermal cap and are based on detailed three-dimensional model output from van Helvoirt (1980) and on numerous sensitivity tests made with our 1DTD cloud model. When substituted into (27) and (28), they directly affect the vertical eddy fluxes and the vertical eddy mixing calculated in the cloud model.

2) SMALL-SCALE VERTICAL MIXING

According to Schlesinger's (1978b) parameterization, the small-scale vertical eddy flux of A superimposed on the triangular profiles is represented by

$$\overline{w^* A^*} = -K_A \frac{\partial \bar{A}}{\partial z}, \tag{30}$$

where $K_\theta = K_v = K_{cw} = 3K_m$ for $A = \theta$, q_v, q_{cw} and $K_r = K_m$ for $A = q_r$. Because of its greater numerical stability, the method of Cotton (1975) is used to represent the vertical eddy flux of vertical momentum as

$$\overline{w^* w^*} = -2K_m \frac{\partial \bar{w}}{\partial z}. \tag{31}$$

The mixing coefficient K_m is given by

$$K_m = \frac{1}{\sqrt{2}} (c\Delta)^2 |\overline{\text{def}}|, \tag{32}$$

with $c = 0.2$ (Schlesinger 1978b),

$$\Delta = (\pi R^2 \Delta z)^{1/3} \tag{33}$$

is the vertical mixing length with R being the radius of the core and Δz being the height increment, and $|\overline{\text{def}}|$ is an area-average estimate of the magnitude of the convective-scale wind deformation tensor following Cotton (1975).

e. Fallout of precipitation

The last term in (13) represents the vertical flux convergence of rain averaged over the horizontal area

of the cell. With the aid of (2), (3), and Leibnitz' rule of integration, this expression becomes

$$\overline{\frac{1}{\rho_e}\frac{\partial}{\partial z}(\rho_e \hat{V}_r q_r)} = \frac{1}{\rho_e R^2}\frac{\partial}{\partial z}(\rho_e R^2 \overline{\hat{V}_r q_r}) - \frac{2}{R}\widetilde{F_r}, \quad (34)$$

(i) (ii)

where $\hat{V}_r$ is the mass-weighted fallspeed associated with a population of raindrops. Term (i) is the convergence of the area-integrated vertical flux of rainwater. To evaluate this term, the area-averaged vertical flux of rain ($\overline{\hat{V}_r q_r}$) must be written as a function of area-averaged quantities. From Lin et al. (1983), the mass-weighted fallspeed for an entire population of raindrops possessing an exponential size distribution following Marshall and Palmer (1948) is

$$\hat{V}_r = \frac{\Gamma(4 + b_r)}{6} a_r \lambda_r^{-br}\left(\frac{p_0}{p_c}\right)^{0.4}, \quad (35)$$

where $a_r = 842\ \text{m}^{1-b}\ \text{s}^{-1}$, $b_r = 0.8$, Γ is the Gamma function, λ_r is the slope of the raindrop size distribution (see appendix A), p_0 is a reference pressure of 1000 mb, and $(p_0/p_c)^{0.4}$ is a factor that allows for the change in fallspeed with air pressure (Foote and DuToit 1969). Multiplying (35) by q_r and averaging over the horizontal area of the cell, we obtain the following expression for the area-averaged vertical flux of rain:

$$\overline{\hat{V}_r q_r} = \zeta_r \hat{V}_r \bar{q}_r, \quad (36)$$

where

$$\zeta_r = \left[\frac{2}{(2 + b_r')y_r}\right]\left(\frac{3}{3 - 2y_r}\right)^{1+b_r'} \times \left[\frac{1 - (1 - y_r)^{3+b_r'}}{(3 + b_r')y_r} - (1 - y_r)^{2+b_r'}\right] \quad (37)$$

and $b_r' = b_r/4$.

Term (ii) in (34) represents the fallout of precipitation if the convective cell is tilted. It reduces the accumulation of condensate that would otherwise occur if the cells were upright. Some runs assume that the model convective cell is tilted at an angle β with respect to the vertical (Fig. 4), such that the air motions follow the axis of the convective cell with raindrops falling in the $-\hat{z}$ direction. The net vertical flux of rain falling across the lateral boundaries of the cell is given by

$$F_r = \frac{1}{2\pi}\int_0^{2\pi} \hat{V}_r[q_r(R, \lambda)] q_r(R, \lambda)(-\mathbf{z}\cdot\mathbf{n}) d\lambda, \quad (38)$$

where $q_r(R, \lambda)$ is the rain content along the cell boundary at azimuth angle λ, $V_r[q_r(R, \lambda)]$ is the mass-weighted fallspeed associated with this local population of raindrops, and $\mathbf{n}$ and $\mathbf{z}$ are unit vectors normal to the cell boundary and in the positive z directions, respectively.

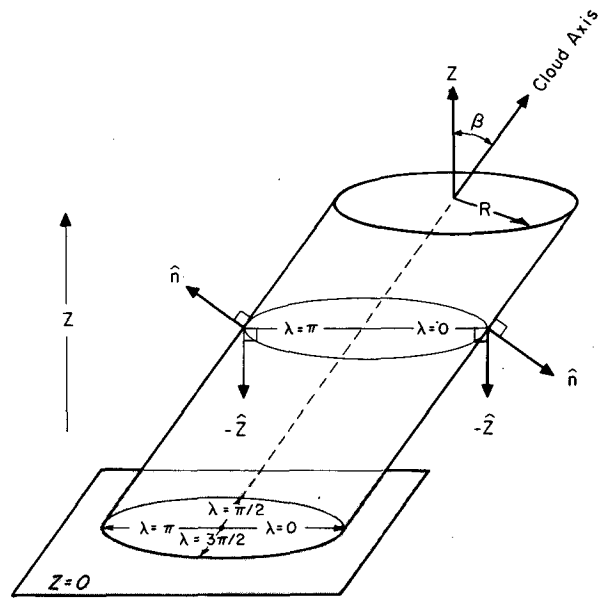

FIG. 4. A depiction of a cylindrically shaped cloud, which is sloped at an angle β from the vertical. The azimuth angle increases in the counterclockwise direction with $\lambda = 0$ defined along the downshear side of the cell. Raindrops are assumed to fall with respect to the cloud in the $-\mathbf{z}$ direction. Because the unit vector $\mathbf{n}$ normal to the tilted cloud boundary changes with λ, the component of the rain flux across the boundary, given by $-\mathbf{z}\cdot\mathbf{n}$, also varies as a function of λ. Note that rain falls out of the cloud and into the environment when $-\mathbf{z}\cdot\mathbf{n} > 0$, and vice versa if $-\mathbf{z}\cdot\mathbf{n} < 0$.

f. Perturbation pressure

Following Raymond (1979), the accelerations in the radial velocity (u) are related to the radial distribution of pressure by the horizontal momentum equation:

$$\frac{du}{dt} = -\frac{1}{\rho_e}\frac{\partial p_c}{\partial r}. \quad (39)$$

Letting $\rho = \rho_e(z)$ and integrating with respect to radius from the cell boundary at $r = R$ to an arbitrary radius within the core at $r = \xi$ ($0 < \xi < R$), the radial distribution of pressure in the convective cell is

$$p_c(\xi) = p_c(R) - \rho_e \int_R^{\xi} \frac{du}{dt} dr, \quad (40)$$

where $p_c(R)$ is the total pressure at the cell boundary. Subtracting the environmental pressure (p_e) from (40), averaging over the horizontal area of the core, and neglecting variations in the azimuthal direction, the area-averaged perturbation pressure becomes

$$\bar{p} = \tilde{p} - \rho_e \frac{2}{R^2}\int_0^R \left[\int_R^{\xi} \frac{du}{dt}(r) dr\right] \xi d\xi. \quad (41)$$

Using (22) to represent $w_r(r)$, rearranging terms, and integrating (4) with respect to radius from the center

of the convective core out to an arbitrary radius r ($r < R$), the lateral distribution of radial velocity is

$$u(r) = -\frac{r}{\rho_e}\left[\frac{1}{2}\frac{\partial}{\partial z}(\rho_e w_0) - \frac{r}{3}\frac{\partial}{\partial z}\left(\frac{\rho_e w_0 \chi}{R}\right)\right]. \quad (42)$$

Further details of the derivation of the pressure perturbation equation are contained in appendix B.

In our approach, the perturbation pressure averaged along the cell boundary, $\tilde{p}$, is the only arbitrary constant in the pressure equation. Holton (1973) and Yau (1979) estimated $\tilde{p}$ using Fourier–Bessel functions to represent the horizontal distribution of perturbation pressure. We believe that our approach gives a more reasonable estimate of $\tilde{p}$, because it is produced from a distribution of $p(r)$ determined explicitly from the profile of $w(r)$ assumed in (22). Since $\tilde{p}$ is the only arbitrary constant, our parameterization also contains a physically understandable link in the horizontal distribution of pressure between the convective cells and their immediate environment.

g. Numerical methods and boundary conditions

The second-order scheme of Crowley (1968) for the advection of w and the "modified upstream differencing" scheme, as described by Soong and Ogura (1973), are used for the advection of θ, q_v, q_{cw} and q_r with a height increment of $\Delta z = 200$ m in all of the model runs. A forward time-differencing scheme similar to Schlesinger (1978a) is used, where the variable time step is

$$\Delta t = \max\left[\frac{0.9}{\mathrm{MAX}\left(\frac{\chi_w \bar{w}}{\Delta z} + \frac{6K_m}{\Delta z^2}\right)}, (\Delta t)_{\max}\right] \quad (43)$$

with $(\Delta t)_{\max} = 5$ s, χ_w given by (27), and MAX the largest value for any interior grid point. This numerical technique has the advantage of maintaining computational stability during periods when intense convection is simulated, and, although some damping by numerical diffusion occurs, it does not appear to be important when compared to the uncertainty associated with any turbulence parameterization in a one-dimensional cloud model.

Figure 5 shows the staggered grid at the vertical boundaries of the model, where $\bar{w} = 0$ is assumed at the top and bottom boundaries (levels $N + 0.5$ and 1.5, respectively). Boundary conditions for the nondimensional perturbation pressure are derived by rearranging the vertical momentum equation in (8) and (9) and letting $\partial\bar{w}/\partial t = 0$ at the boundaries, giving

$$\frac{\overline{p_2} - \overline{p_1}}{\Delta z} = (R_d\theta_{ve})^{-1}_{1.5}\left[\bar{B}_{1.5} - \frac{(\rho_e R^2 \overline{ww})_2}{(\rho_e R^2)_{1.5}\Delta z}\right] \quad (44)$$

$$\frac{\bar{p}_{N+1} - \bar{p}_N}{\Delta z} = (R_d\theta_{ve})^{-1}_{N+0.5}\left[\bar{B}_{N+0.5} + \frac{(\rho_e R^2 \overline{ww})_N}{(\rho_e R^2)_{N+0.5}\Delta z}\right] \quad (45)$$

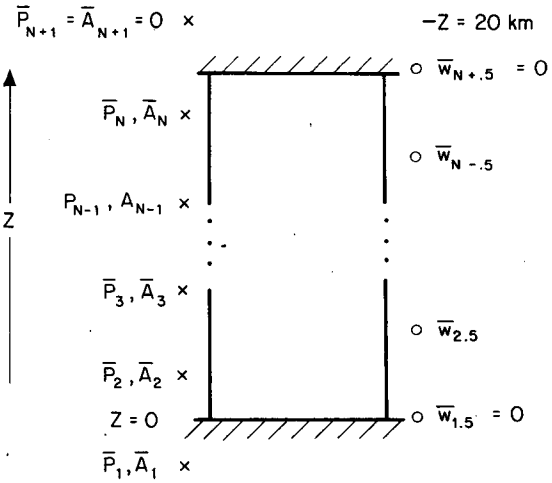

FIG. 5. The staggered grid used in the modified upstream differencing scheme at the top and bottom boundaries.

at the lower and upper boundaries, respectively. In (45), $\bar{P}_{N+1}$ is set to zero in order to prevent the development of an implied vertical pressure gradient above the top of the model domain.

A prognostic equation based on (8) is used to calculate θ and q_v at the surface, where, if A represents θ and q_v, then

$$\frac{\partial\bar{A}_1}{\partial t} = \frac{(\rho_e R^2)_2[\bar{w}_2\tilde{A}_1 - (\overline{wA})_2]}{(\rho_e R^2)_1\Delta z}. \quad (46)$$

The horizontal divergence and the vertical flux transports of θ and q_v were considered in deriving (46) because of the importance of the convective downdrafts in transporting air down to the surface. As displayed in Fig. 5, the values of $\bar{\theta}$, $\overline{q_v}$, $\overline{q_{cw}}$ and $\overline{q_r}$ are set to zero at the upper boundary.

3. Initial conditions and initiation of convection

All model runs are initialized using the vertical profiles of temperature and water vapor mixing ratio taken from the 1200 UTC sounding aboard the Canadian RV *Quadra* on Day 261 (18 September 1974) of GATE (see Fig. 6). The data are taken from the Final Upper Air DataSet prepared by the Convection Subprogram Data Center (CSDC).[1] This sounding was selected so that the output from the model could be compared with previously published observational studies of the events on this day (Warner and Austin 1978; Warner et al. 1979, 1980; Frank et al. 1981) and with three-dimensional model simulations of the deep clouds that occurred (Simpson and van Helvoirt 1980; Simpson et al. 1982, 1986).

[1] Available from National Climatic Center, Asheville, NC 28801.

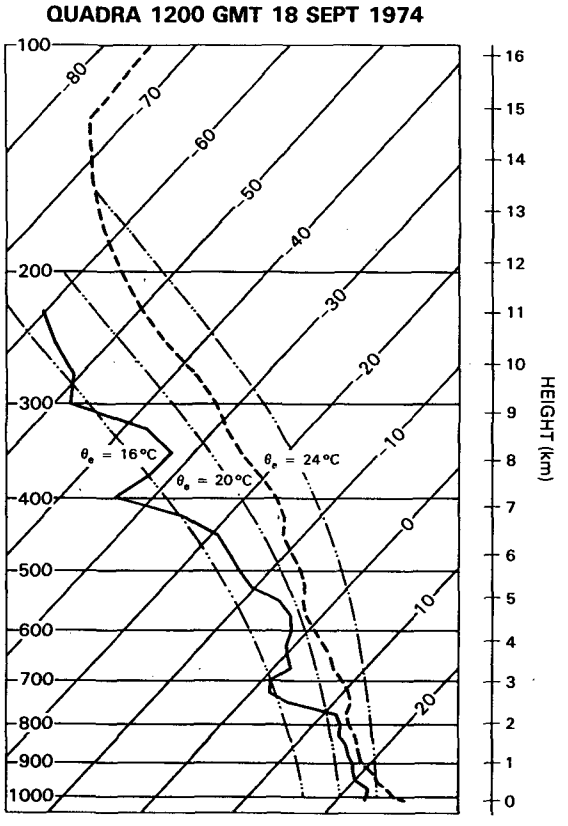

FIG. 6. Skew T–log$P$ plot of the 1200 UTC sounding taken aboard the *Quadra* research vessel on day 261 of GATE. Temperatures and dewpoint temperatures are denoted by the heavy dashed and solid curves, respectively. Light dash–dot lines are moist adiabats.

It appears that the dominant means by which deep tropical convective clouds are initiated is the lifting of low-level air near the ocean surface by gust fronts associated with cumulus convection that is already present (Simpson 1980; Houze and Betts 1981; Tao and Simpson 1984; Tao and Soong 1986; Nicholls 1987). Convection in the model is therefore initialized by applying a sustained forcing below cloud base (600 to 700 m above the ocean) that is consistent with the forced ascent associated with tropical maritime gust fronts (Emmitt 1978; Frank et al. 1981; Addis et al. 1984). The vertical profile of $\bar{w}$ increases parabolically from 0 m s^{-1} at the surface to 2 m s^{-1} at $z = 0.4$ km. Starting the model simulations from an initially quiescent state (i.e., $\bar{w} = 0$ everywhere), the subcloud forcing is increased linearly with time during the first 100 s and remains at full strength for the next 1100 s. This period of low-level forcing is needed to simulate maximum cloud-top heights consistent with those observed on this day (Warner et al. 1980; Simpson et al. 1986). The duration of the forcing is reasonable given the slow movement of the convective towers relative to the gust fronts (Warner et al. 1980) and the rate at which convection was initiated (Tao and Simpson 1984). After the first 20 min, the forcing is no longer applied and changes in $\bar{w}$ at $z \leq 0.4$ km are then predicted using the vertical momentum equation. Imposing the low-level forcing in this way prevents the development of unrealistically large perturbation pressures that would occur if the forcing was applied instantaneously as an initial condition.

In the real atmosphere, forced ascent of air at low levels would be provided by the vertical pressure gradients that form in response to strong convergence at the gust front. These pressure gradients are diagnosed in the model by rearranging the vertical momentum equation in the same manner as in section 2g, such that

$$\frac{\partial \bar{p}}{\partial z} = (R_d \theta_{ve})^{-1} \left[\bar{B} - \frac{\partial \bar{w}}{\partial t} - \left(\frac{\partial \bar{w}}{\partial t} \right)_{\text{adv}} \right], \quad (47)$$

where $\bar{B}$ is calculated by the model and the other terms in brackets are determined by the specified forcing. Although this method can be used instead of (41) to calculate the perturbation pressure, its purpose here is to illustrate that balance between the pressure and momentum fields is maintained in areas of forced ascent.

4. Design of model experiments

The conditions used in the control run are summarized in Table 2. Although numerous simulations were made to test the sensitivity of the model to each of these conditions, only a much smaller, representative sample of the runs will be discussed. All of the runs will be compared with the control run (run I) for the purpose of examining how each of the following physical mechanisms affect the structure of the simulated cells:

- dynamic entrainment (runs II, III and VII),
- lateral eddy mixing (run VIII),
- horizontal profiles of dependent quantities and inclusion of a thermal-cap circulation (runs IV and V),
- precipitation fallout (run VI),
- magnitude of low-level, sustained forcing (runs IX and X),
- duration of low-level, sustained forcing (runs XI and XII).

TABLE 2. Characteristics of control run.

Cloud radius decreases with height below 4 km following (16).
Lateral eddy mixing is neglected.
Small-scale vertical eddy mixing is parameterized.
A thermal-like circulation is parameterized below cloud top using the horizontal profiles in Table 1.
The cell has no slope ($\beta = 0°$).
No rain enters the cloud from the environment [$(q_r)_i = 0$].
Pressure perturbation is parameterized.
A maximum forcing of $\bar{w} = 2$ m s^{-1} is sustained at $z = 0.4$ km during the first 20 min of the simulation.

The following section contains a detailed discussion of the convection simulated in the control run, as well as results from the other simulations.

5. Results

a. Control case

Figure 7 shows the time–height plots of $\bar{w}$, $\bar{\theta}$ and $\overline{q_v}$ for the control case. The updraft grows rapidly during the first 25 min of the simulation as air from the boundary layer rises into the cell during the period of sustained low-level forcing. Maximum updraft speeds of 10.3 m s^{-1} are reached at 25 min. The top of the updraft, defined by the upper contour of $\bar{w} = 1$ m s^{-1}, grows at a rate of 4 m s^{-1} during the first 15 min and is followed by a more active growth phase between 15 and 35 min where the rate of rise approaches 9 m s^{-1}. A peak cloud-top height (defined by the height of the $\overline{q_L} = 0.1$ g kg^{-1} isoline) of 13 km is reached by $t = 38$ min. The fields of $\bar{\theta}$ and $\overline{q_v}$ displayed in Figs. 7b and 7c show that the air in the region of active updraft is generally warm and moist with maximum values of $\bar{\theta} = 2.8$°C and $\overline{q_v} = 5.0$ g kg^{-1}. These maximum values compare well with output from the three-dimensional model simulations of Simpson et al. (1982, 1986), in which maximum values of $w = 7.7$–11.2 m s^{-1} and $\theta = 2.8$°–3.4°C were simulated for deep convection (cumulonimbus AA in Simpson et al. 1986) that extended up to 13.2–15.6 km (output provided by M. McCumber).

After the low-level forcing is turned off (at $t = 20$ min), the updraft starts to erode rapidly at all levels below the height of maximum ascent and is cut off from the boundary layer between 25 and 40 min as downdraft develops from below. A weak and shallow downdraft persists below 1.5 km with maximum descent of -1.5 m s^{-1} occurring at $z = 0.4$ km. Although there is little difference in temperature between the air in the downdraft and the environment (see Fig. 7b),

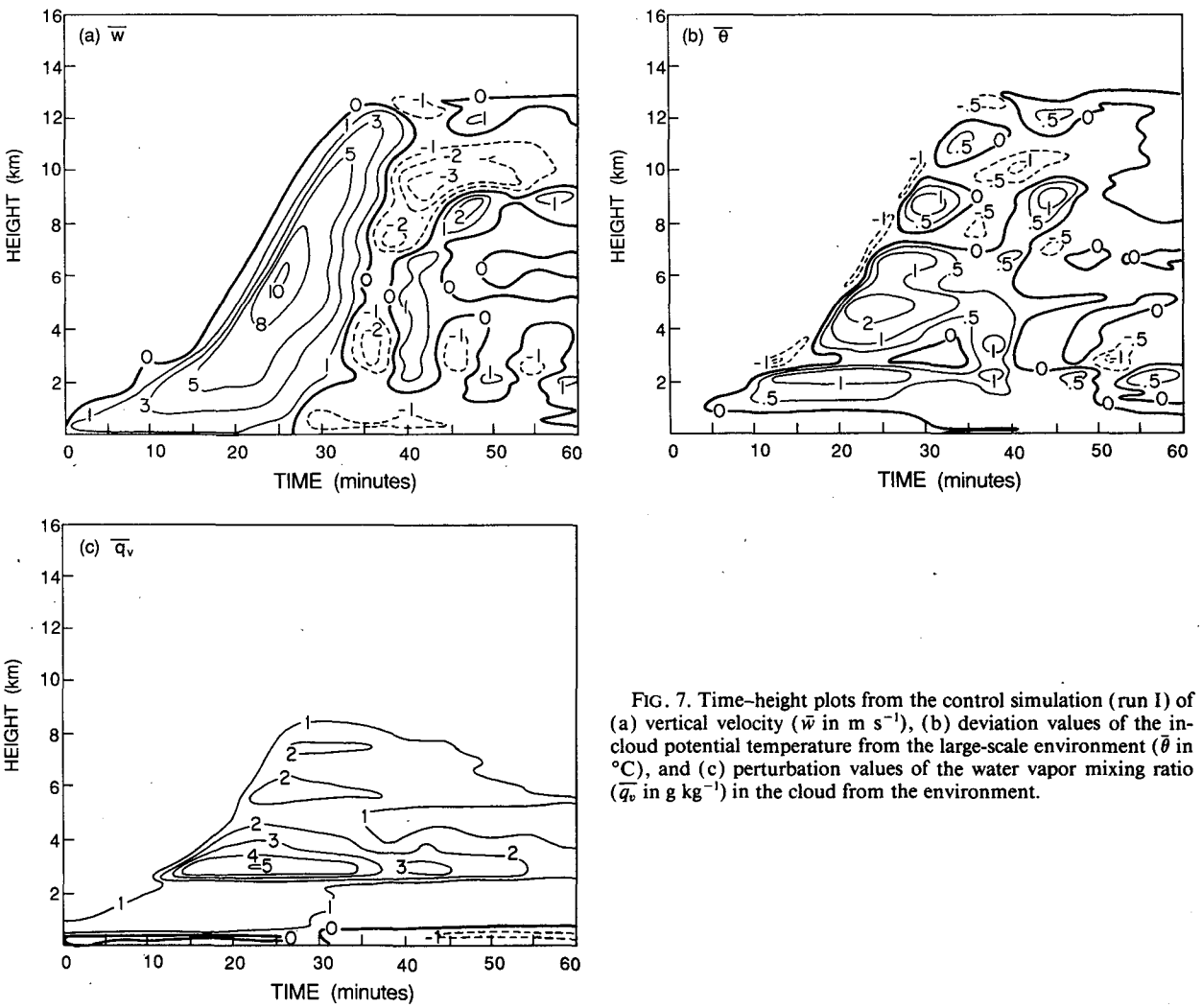

FIG. 7. Time–height plots from the control simulation (run I) of (a) vertical velocity ($\bar{w}$ in m s^{-1}), (b) deviation values of the in-cloud potential temperature from the large-scale environment ($\bar{\theta}$ in °C), and (c) perturbation values of the water vapor mixing ratio ($\overline{q_v}$ in g kg^{-1}) in the cloud from the environment.

Fig. 8a shows that the downdraft at low levels is negatively buoyant due mainly to the water loading associated with rain (in Fig. 10b) and the downward transport of drier air (Fig. 7c). After 35 min, the downdraft is capped by a stable buoyancy oscillation in the 2.0–3.5 km layer (see Fig. 8a).

One of the reasons for the rapid decay of the updraft after 25 min is the reduction of cell buoyancy by water loading. With positive anomalies in $\bar{\theta}$ and $\overline{q_v}$ seen in Figs. 7b and 7c below 7 km and from 30 to 35 min, Fig. 8a shows that the cell is still negatively buoyant because of the large accumulation of rain in this region (Fig. 10b). Since only weak vertical pressure-gradient forces are present in Fig. 11b, one can conclude that excessive precipitation loading is responsible for the rapid formation of these downdrafts. This is confirmed in a simulation in which downdraft failed to develop below 4 km when rain was not allowed to form.

The lateral entrainment of environmental air into the cell also contributes to the extensive deterioration of the updraft. Dividing term (ii) in (8) by $-\tilde{A}$ gives the rate of dynamic entrainment (negative values denote radial inflow into the convective core) and detrainment (positive values represent radial outflow from the cell) shown in Fig. 8c. During the first 25 min, entrainment occurs gradually throughout a deep layer below the height of maximum vertical velocity, whereas the detrainment rates are larger and concentrated in a shallow layer between the level of maximum updraft speed and cloud top. The deleterious effect of horizontal entrainment upon cloud growth is exemplified by the steady decrease in $\bar{\theta}$ with time in the 3–5 km layer after $t = 25$ min. Several experiments in the following subsection will demonstrate the sensitivity of the model to how dynamic entrainment is parameterized.

Figure 8c shows that cell detrainment occurs after 25 min in limited layers at 2.2–2.8 km, 5.0–5.6 km, 6.8–7.4 km, and 9.2–10.0 km. These detrainment layers correspond to well-defined dry, stable layers in the environment at 2.2–2.8 km and 6.8–7.4 km and to less-defined stable layers at 5.0–5.6 km and 8.8–10.0

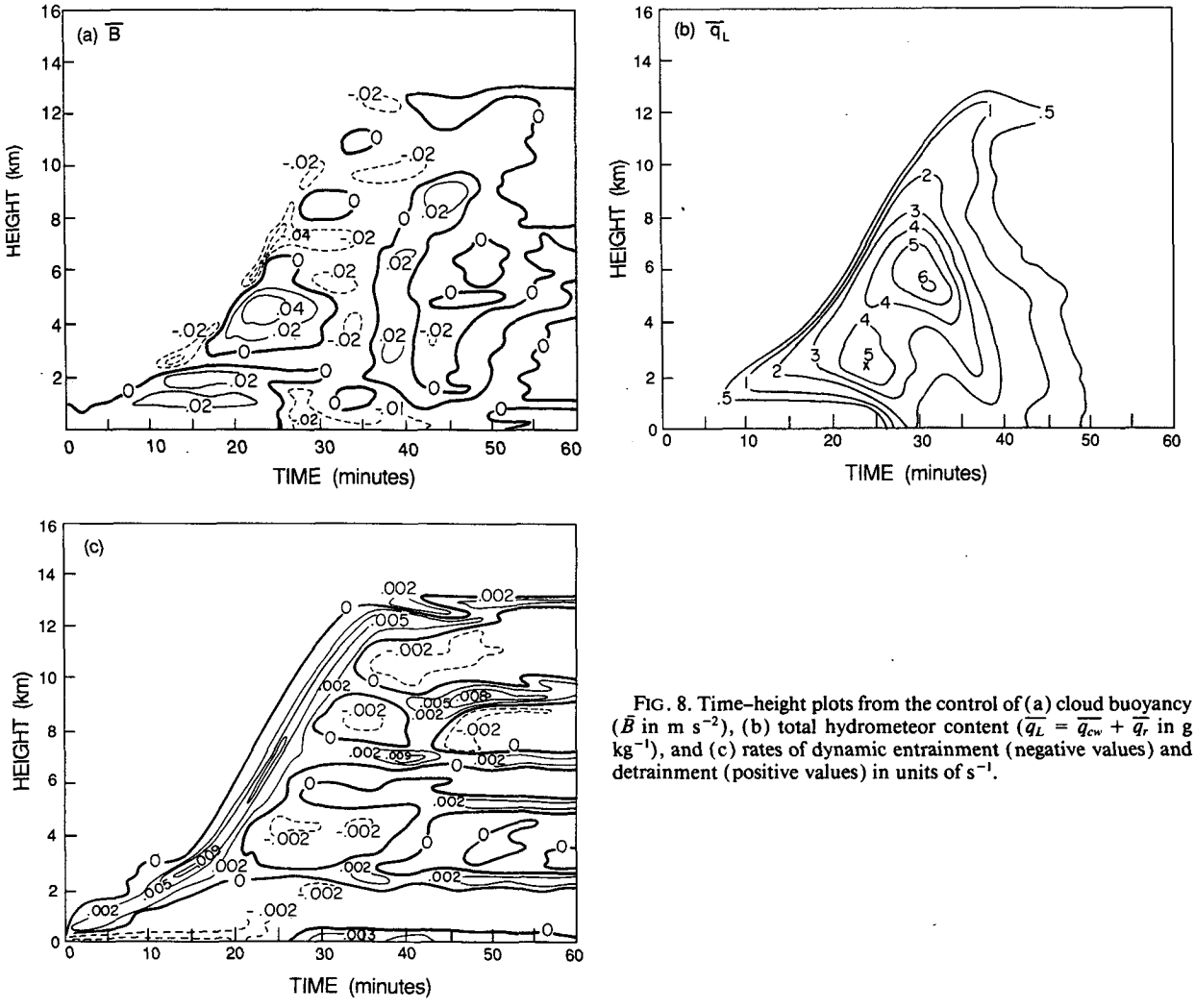

FIG. 8. Time–height plots from the control of (a) cloud buoyancy ($\bar{B}$ in m s^{-2}), (b) total hydrometeor content ($\overline{q_L} = \overline{q_{cw}} + \overline{q_r}$ in g kg^{-1}), and (c) rates of dynamic entrainment (negative values) and detrainment (positive values) in units of s^{-1}.

km (see Fig. 6). The profile of condensate detrained from the cell (Fig. 9a) is enhanced near these distinct layers, with the greatest detrainment of condensate occurring from 2.4–3.3 km. These results agree closely with the observations on GATE day 261 of extensive patches of stratus and stratocumulus persisting between 2.5 and 5.0 km (Warner et al. 1979).

The input sounding also accounts for the complex structure of the $\bar{\theta}$ and $\overline{q_v}$ fields in Figs. 7b and 7c. Maxima in $\bar{\theta}$ and minima in $\overline{q_v}$ occur at the base of the stable layers (2.2, 4.8, 6.6, and 8.8 km), and the minima in $\bar{\theta}$ and maxima in $\overline{q_v}$ occur at the top of the stable layers (2.8, 5.6, 7.4 and 10.0 km). Since the environment immediately beneath the stable layers is close to moist adiabatic, the differences in the water vapor mixing ratios between the cell (at water saturation) and the environment (near saturation) are smallest at the bottom of the stable layers.

The strength of the 2.2–2.8 km stable layer has a particularly important impact upon the convection, where the intensity of the updraft and the rate of rise of the cloud-top increase after the convective cell penetrates above 3 km at 15 min (see Fig. 7a). From Fig. 9b, the total condensation in the cell is greatest from 1.0 to 2.4 km and from 3.0 to 5.0 km where the moist, unstable layers are located, while most of the evaporation occurs below 1.0 km and in the dry, stable layer between 2.4 and 3.0 km.

The highest cloud water contents (Fig. 10a) occur in the upper part of the updraft throughout its growth stage (regions R_2 and R_3), while the largest rainwater contents (Fig. 10b) develop 7–9 min later at lower levels in the cell (region R_1).

The maximum in $\overline{q_r}$ at 2.4 km and 25 min occurs where the updraft collapses shortly after the low-level forcing is terminated at 20 min. Although autoconversion of cloud water into rain (PRAUT) is important in the initial production of rain, the rapid increase in rainwater after its initiation is due almost entirely to the collection of cloud water (PRACW). Since cloud water is no longer produced after the downdraft develops, the rain falls to the surface with no further increase in concentration.

This maximum in $\overline{q_r}$ is also seen as a maximum in radar reflectivity in Fig. 10c, where the equivalent radar reflectivity factor for rain is calculated, following Leary and Houze (1979), as

$$Z = 6.675 \times 10^7 (\rho_e q_r)^{1.25} \tag{48}$$

with the units of $(\rho_e q_r)$ being in kilograms per cubic meter. The subsequent fall of rain to the surface produces the intense peak in surface rainfall rate shown in Fig. 10d of 55 mm h^{-1} at 30 min. Because the 0°C level is located at $z = 4.5$ km, this feature is due strictly to warm-rain processes. The peak surface reflectivities are in good agreement with Szoke et al. (1986) and Szoke and Zipser (1986), while the maximum surface rainfall rate is consistent with Warner and Austin (1978) when the differences in horizontal resolution are taken into consideration. Although the difference in time between the first 20 dBZ echo aloft and the 40

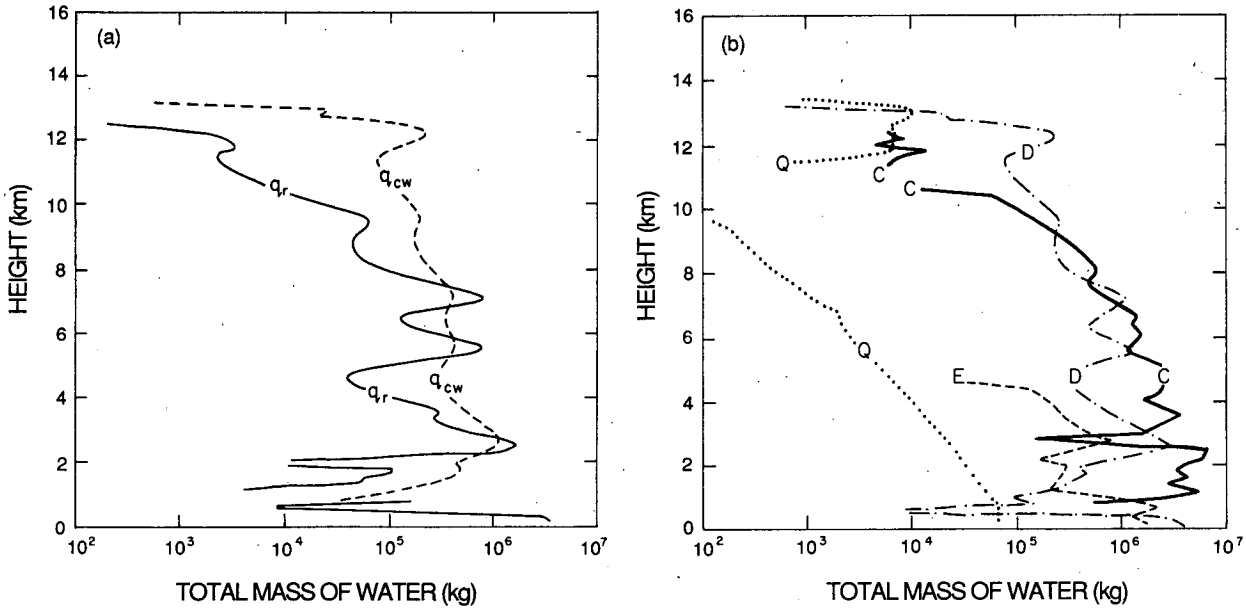

FIG. 9. (a) Vertical profiles of the total mass in kg of cloud water (q_{cw}, dashed line) and rain (q_r, solid line) detrained from the cell as a function of height in the control run. (b) Vertical profiles of the total mass in kg of condensation (C, solid line), evaporation below the 0°C level (E, dashed line), and detrained condensate (D, dash-dot line) accumulated over the lifetime of the convective cell. Q (dotted line) represents the total mass of condensate suspended aloft in the cell at the end of the simulation.

dBZ surface echo is about 5 to 10 min longer than found by Szoke and Zipser (1986), the difference in time between the first echo aloft and the maximum surface rainfall (20 min) is in exact agreement with their findings. One reason for this may be in neglecting wind shear effects, which would allow some rain to fall immediately out of the updraft and reach the surface sooner than is currently simulated.

The second maximum in $\overline{q_r}$ at 5.4 km and 32 min is associated with the region of strongest updraft, which occurred at a somewhat higher altitude (6 km) a few minutes earlier (24 min). The rapid decrease in the strength of the updraft between 4 and 7 km, due in part to the effects of excess water loading forced by the accumulating rainwater, causes the base of the maximum concentration of raindrops to begin to fall between $t = 25$ and 30 min. The drops in the region grow by collecting cloud water until the updraft dissipates and condensation ceases by 32 min. Thereafter, the high concentration of rain falls rapidly to the surface and produces the secondary peak in the surface rainfall rate of 37 mm h^{-1} at 40 min (Fig. 10d). Because the growth of these drops occurred above the freezing level, ice-phase processes are likely to have been important in the real atmosphere. They would be expected to lower the reflectivities above the 4 km level and alter the surface rainfall rates after 35 min. An ice-phase parameterization similar to that of Lin et al. (1983) and Rutledge and Hobbs (1984) has been added to the model and will be used in future studies to examine the role of ice processes in tropical and midlatitude squall-convection. Despite the lack of an ice-phase scheme in the present model, the maximum height of the 29 dBZ echo exceeds 10 km, which agrees well with the largest heights observed by Warner and Austin (1978) at times nearest 1200 UTC 18 September 1974.

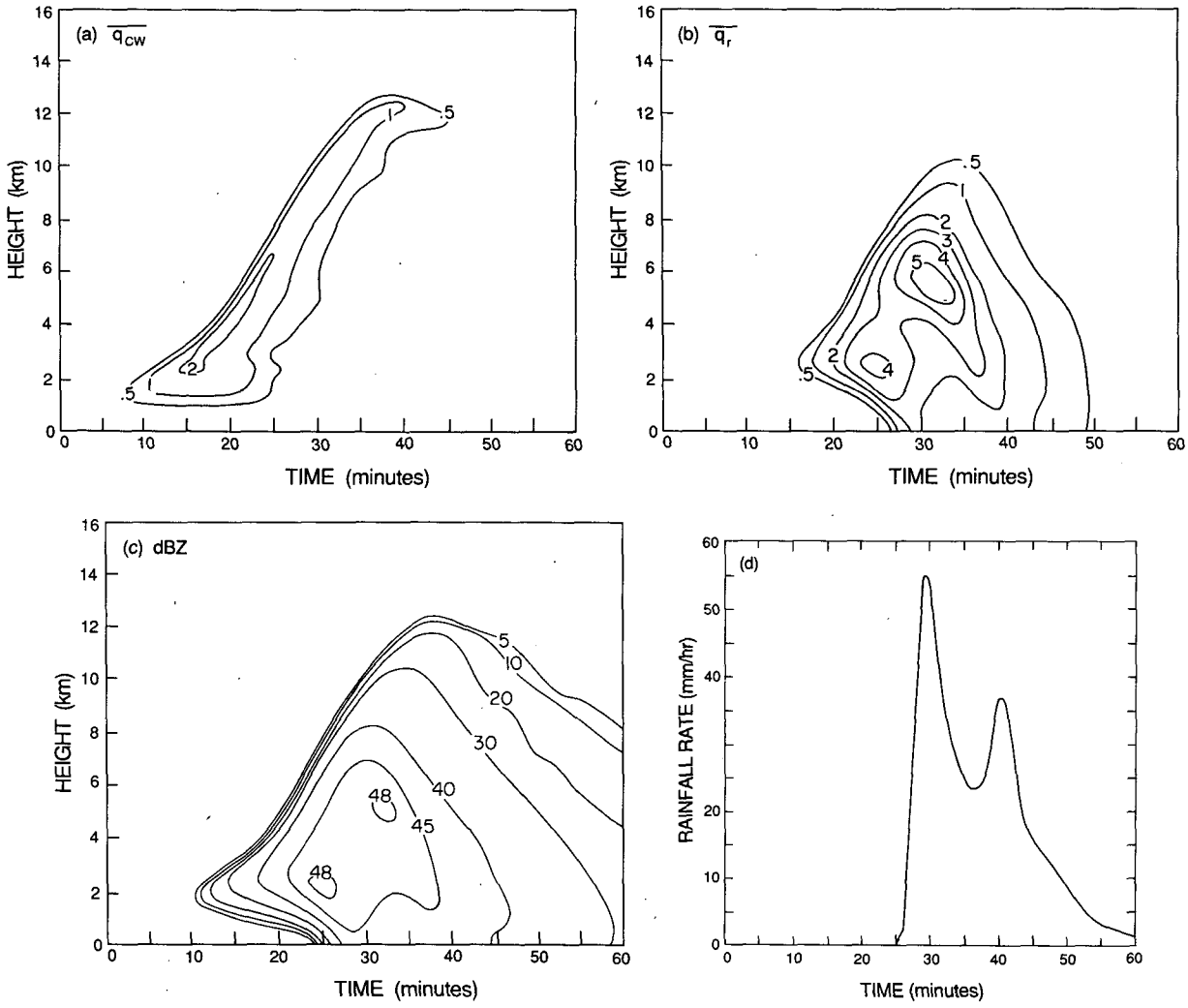

FIG. 10. Time–height plots from the control run of (a) cloud water in g kg^{-1}, (b) rain in g kg^{-1}, and (c) equivalent radar reflectivity in dBZ. In (d), surface rainfall rates (in mm h^{-1}) are shown as a function of time.

The perturbation pressure ($\bar{p}$) and its contribution to the vertical momentum through the vertical perturbation pressure force are shown in Fig. 11. The upward pressure force below 0.4 km for the first 20 min is needed to support the low-level sustained forcing in accordance with (47). The large perturbation pressure below 0.4 km at 25–45 min acts to slow the downdraft as it approaches the surface. The perturbation pressure is small and unimportant everywhere else except near the top of the growing convective cell, where large, excess perturbation pressures occur in the center of the thermal cap region. The resultant vertical pressure force is downward in the lower part of the thermal cap region (R_2) and upward in region R_3 near cloud top. This pressure force opposes the cell buoyancy, which is positively buoyant in R_2 and negatively buoyant in R_3. The most important effect of the pressure perturbation is to reduce the rate at which the updraft decelerates with height as it penetrates into the upper troposphere. It will be shown in the following subsection that incorporating a thermal circulation at cloud top is very important in determining the vertical distribution of perturbation pressure needed to model deep convection above 10 km.

b. *Sensitivity tests*

In designing an improved one-dimensional cumulonimbus model, numerous simulations were conducted that tested the sensitivity of the model to changes in how a variety of physical processes were parameterized. A list describing all of the sensitivity tests is given in Table 3; runs II–XII are identical to the control case (run I), except as indicated in Table 3. The maximum values of key parameters resulting from runs I–XII are given in Table 4. From these 12 simulations, most of the discussion will focus on a subset of five sensitivity tests (runs II through VI), representing the most important physical processes found to affect the growth and internal structure of GATE cumulonimbus updrafts.

TABLE 3. Description of model sensitivity tests that differ from the control run.

Run	Description
I	Control run.
II	Constant cloud radius of $R(z) = R_0 = 1$ km, top-hat cell profiles ($x = y_\theta = y_{vc} = y_{cw} = y_r = 0$), and no cloud-top thermal circulation.
III	Constant cloud radius ($R_0 = 1$ km).
IV	Cell profiles are top-hat shape ($x = y_\theta = y_{vc} = y_{cw} = y_r = 0$) with cloud-top thermal circulation.
V	Cell profiles are triangular in shape ($x = y_\theta = y_{vc} = y_{cw} = y_r = 1$) with no cloud-top thermal circulation.
VI	Cell sloped at $\beta = 45°$.
VII	$A_c = \bar{A}$ instead of A_e during entrainment.
VIII	Lateral eddy mixing is included according to (18).
IX	Low-level forcing reduced to 1 m s^{-1}.
X	Low-level forcing increased to 3 m s^{-1}.
XI	Duration of low-level forcing reduced to 5 min.
XII	Duration of low-level forcing increased by 5 min.

The model in run II resembles the 1DTD parameterizations used by Cotton (1975) and Randall and Huffman (1982) in assuming that the radius of the cell is constant with height, no thermal-like circulation is parameterized near cloud top, and dependent quantities in the model are represented by top-hat profiles. As Fig. 12 shows, the convection was very weak and failed to penetrate above the 4.5 km level in the presence of sustained gust-front forcing. The only way that deep clouds can be simulated in this type of model structure is to destabilize the observed environment in an unrealistic manner, such as by imposing large-scale lifting to the sounding to bring the environment close

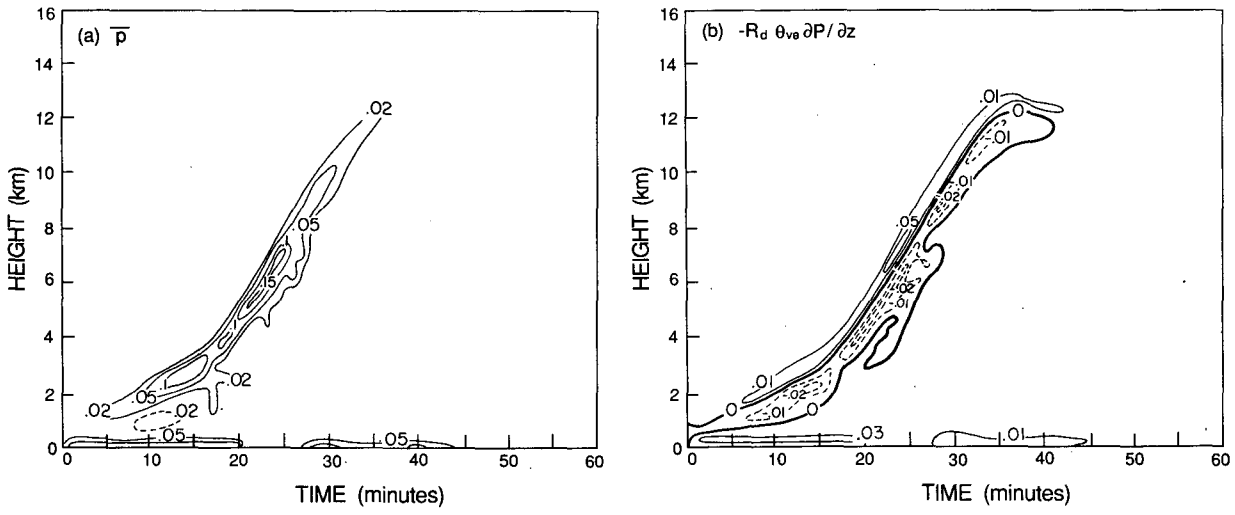

FIG. 11. Time–height profiles from the control run of (a) perturbation pressure ($\bar{p}$ in mb) and (b) its vertical gradient ($-R_d\theta_{ve}\partial\bar{P}/\partial z$ in m s^{-2}).

TABLE 4. Results from sensitivity tests.

Run	Maximum values							
	Z_T (km)	$\bar{w}$ (m s^{-1})	$\bar{\theta}$ (°C)	$\overline{q_L}$ (g kg^{-1})	$\overline{q_{cw}}$ (g kg^{-1})	$\overline{q_r}$ (g kg^{-1})	dBZ$_e$ (dBZ)	RR (mm h^{-1})
I	13.0	10.3	2.9	6.1	2.5	5.8	48.4	55.1
II	4.2	5.5	1.5	3.0	1.9	2.1	44.9	29.9
III	7.1	6.0	1.9	3.1	2.1	2.4	45.4	41.7
IV	7.3	11.6	2.5	5.0	2.3	4.2	48.0	45.3
V	7.9	9.4	2.5	4.9	2.5	4.1	48.2	54.6
VI	14.7	11.5	3.0	5.0	2.5	4.0	46.4	18.5
VII	16.9	25.2	5.7	11.1	2.6	10.8	51.5	128.6
VIII	5.7	4.5	1.2	2.7	1.9	1.7	43.5	17.4
IX	5.7	4.2	1.2	2.7	1.9	1.6	42.9	18.1
X	15.8	18.1	3.6	9.3	2.7	9.0	51.0	105.6
XI	8.1	7.6	2.1	4.0	2.4	3.3	46.8	40.6
XII	14.5	11.0	2.9	7.7	2.5	7.5	49.7	63.2

to saturation or to initiate convection in the model using unrealistically intense low-level forcing that has no known origin in the tropical atmosphere.

Run III differs from the control case only by assuming a constant cell radius with height (Fig. 1a) rather than the vertically varying cell radius (Fig. 1b). Compared to the control case, cell buoyancies were smaller and the updraft was weak (compare Figs. 13a and 13b with Figs. 7a and 8a). The vertical growth rate of the updraft was much slower and the cloud reached a maximum height of only 7 km. Although the updraft speeds were much less in this run, the rates in which environmental air was dynamically entrained through the sides of the convective core were almost exactly the same in both runs (Figs. 8c and 13c). Thus, because the sides of the updraft were constrained to be cylindrical, the dynamic entrainment of environmental air in run II was much more effective in reducing the updraft buoyancies and prevented the cell from developing into a deep cumulonimbus cloud. This sensitivity test illustrates the importance of properly representing the effects of lateral entrainment, which is determined here by the shape of the updraft at lower levels. The decreasing radius with height assumed in the control run, which corresponded to observations of GATE updrafts (Zipser and LeMone 1980), produces less entrainment and consequently a more realistic deep cloud.

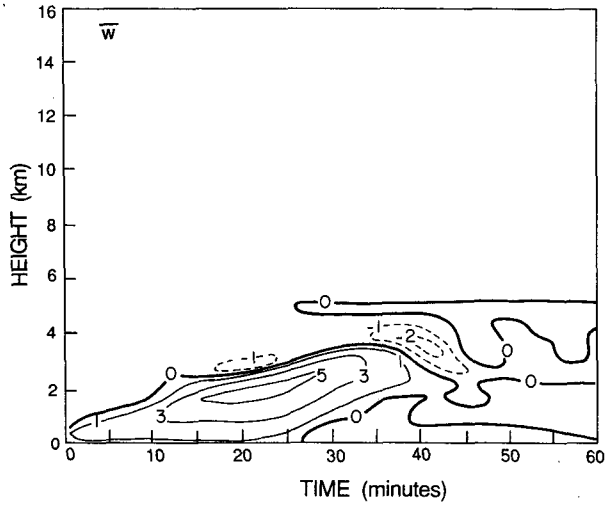

FIG. 12. Time-height plot of $\bar{w}$ in m s^{-1} for run II.

Top-hat profiles of model-dependent quantities are assumed in run IV, and no thermal-like circulation near cloud top is included. Thus, the methods used to represent area-averaged vertical fluxes and perturbation pressure in this run are similar to those that have been used in previous 1DTD models, while dynamic entrainment is parameterized in the same way as in the control case through the use of a variable cell radius. The convection that developed failed to grow above 8 km due to the slow vertical growth of the updraft, even though the updraft speeds were slightly larger than in the control case (Fig. 14). Note also the very rapid decrease in vertical velocity with height below cloud top, which, as will be shown in the following run, was due to the way the perturbation pressure field was parameterized near cloud top.

Run V is like run IV in that the cloud-top thermal is again not included. However, triangular-shaped profiles are assumed instead of top-hat profiles for each of the dependent quantities. The updraft that was produced (see Fig. 15a) again failed to penetrate beyond the 8 km level, despite having peak vertical velocities that exceeded 9 m s^{-1}. As in run IV, the updraft decreased very rapidly with height from its maximum value located about 1 km below cloud top to zero at cloud top, thus producing a very thin, intense layer of strong divergence near cloud top. The reason for the abrupt halting of the updraft can be seen in the vertical distribution of perturbation pressure near cloud top,

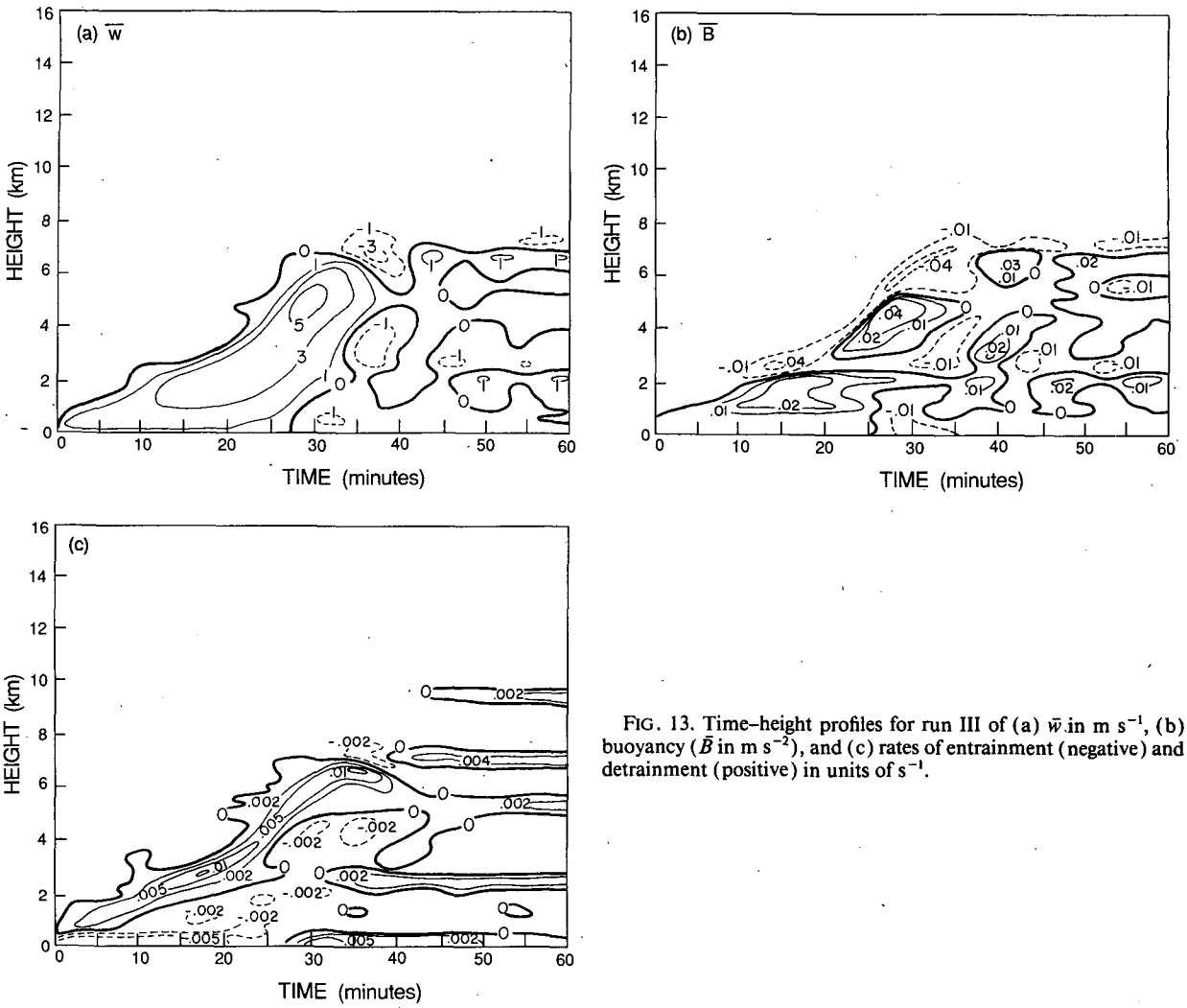

FIG. 13. Time–height profiles for run III of (a) $\bar{w}$ in m s^{-1}, (b) buoyancy ($\bar{B}$ in m s^{-2}), and (c) rates of entrainment (negative) and detrainment (positive) in units of s^{-1}.

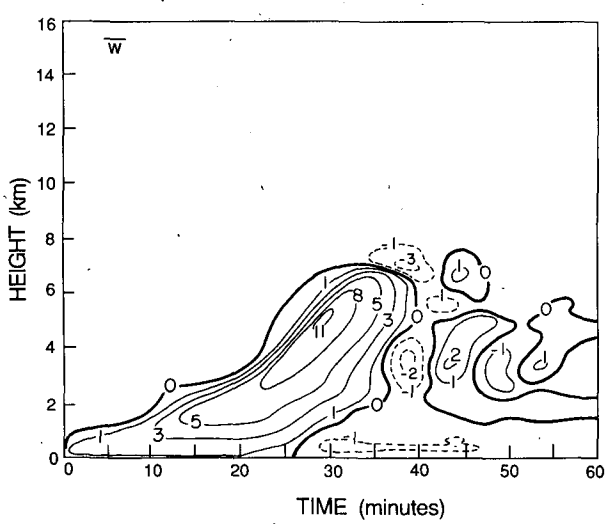

FIG. 14. As in Fig. 12, except for run IV.

where, as Fig. 15b shows, negative pressure perturbations occurred about 1 km below cloud top in region R_2 of the cell with excess perturbation pressures located in region R_3. Very strong downward pressure forces thus occurred in the center of the cloud-top region, and these forces inhibited the vertical growth of the convective cell.

But when the thermal circulation was included in the model, as in the control run (see Fig. 11), positive perturbation pressures persisted throughout both cloud-top regions R_2 and R_3, which produced strong upward pressure forces in R_3 (and weaker downward pressure forces in R_2) of the cell. These forces help to reduce the downward accelerations in the updraft by opposing the negative buoyancies at cloud top (Fig. 8a). The thermal-cap circulation is a realistic feature seen in the real atmosphere, in laboratory thermals, and in three-dimensional cloud models. It develops at least partially in response to the forces (or "form drag") that act on

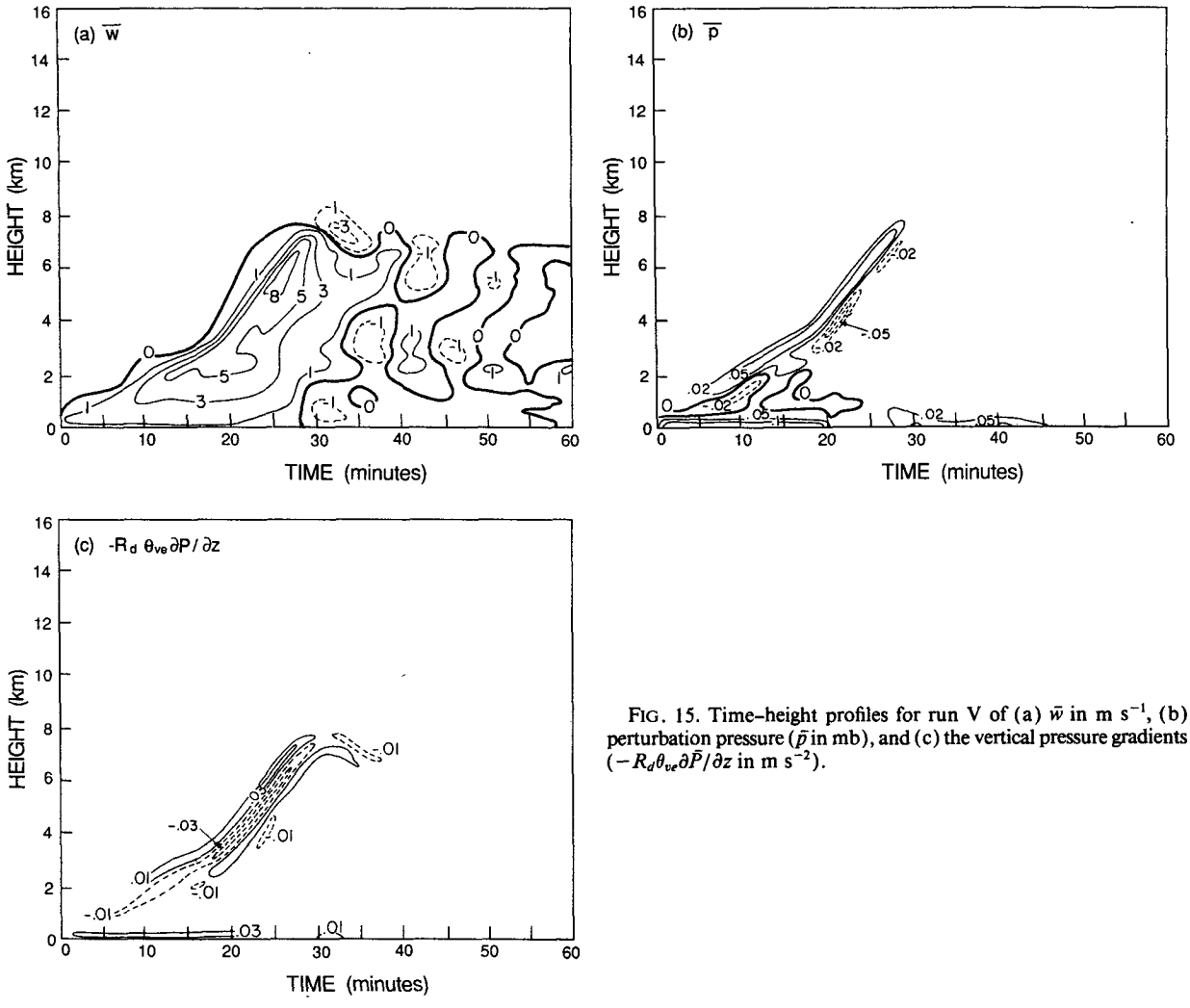

FIG. 15. Time-height profiles for run V of (a) $\bar{w}$ in m s^{-1}, (b) perturbation pressure ($\bar{p}$ in mb), and (c) the vertical pressure gradients ($-R_d\theta_{ve}\partial\bar{P}/\partial z$ in m s^{-2}).

the convective cell as it rises in a motionless atmosphere. In previous one-dimensional models, it was expected that the perturbation pressures would be properly diagnosed without regard for the detailed representation of the horizontal distribution in vertical velocity across the cell. But in comparing runs IV and V with the control run, the removal of the overturning thermal cap region has a dramatic effect upon the vertical distribution of pressure perturbation near cloud top, such that the vertical development of the simulated convection is severely hampered by the vertical pressure gradient if a somewhat realistic thermal-cap circulation is not included in the calculation of pressure perturbation.

As a crude means of parameterizing wind shear, the convective cell in run VI was assumed to be tilted 45° from the vertical in order to test the sensitivity of the model to the fall of precipitation out of sloped updrafts. Compared to the control case, the updraft that developed in this run (Fig. 16a) was stronger, deeper, and lasted 5–10 min longer at mid- to-upper levels. Because rain was permitted to fall out of the tilted updraft, the total condensate in the updraft below 8 km (Fig. 16b) was 1–1.5 g kg^{-1} less than in the control run. The reduced water loading in the sloped cell resulted in higher buoyancies (Fig. 16c), which slowed the rate of decay of the updraft, reduced the rates of dynamic entrainment at the base of the updraft, and delayed the formation of the downdraft at low-to-mid levels. These combined to produce higher excess temperatures (Fig. 16d) and buoyancies that allowed the updraft to be stronger and more persistent in time at middle and upper levels.

In run VII, an undiluted, adiabatic updraft was simulated by assuming the dynamically entrained air had the same thermodynamic properties as in the convective cell. As Table 4 indicates, the intensity of the simulated updraft is larger than the strengths of the updrafts observed by aircraft flights through GATE clouds (LeMone and Zipser 1980; Zipser and LeMone 1980). This result suggests that some lateral entrainment occurs in most GATE cells, including ones that overshoot

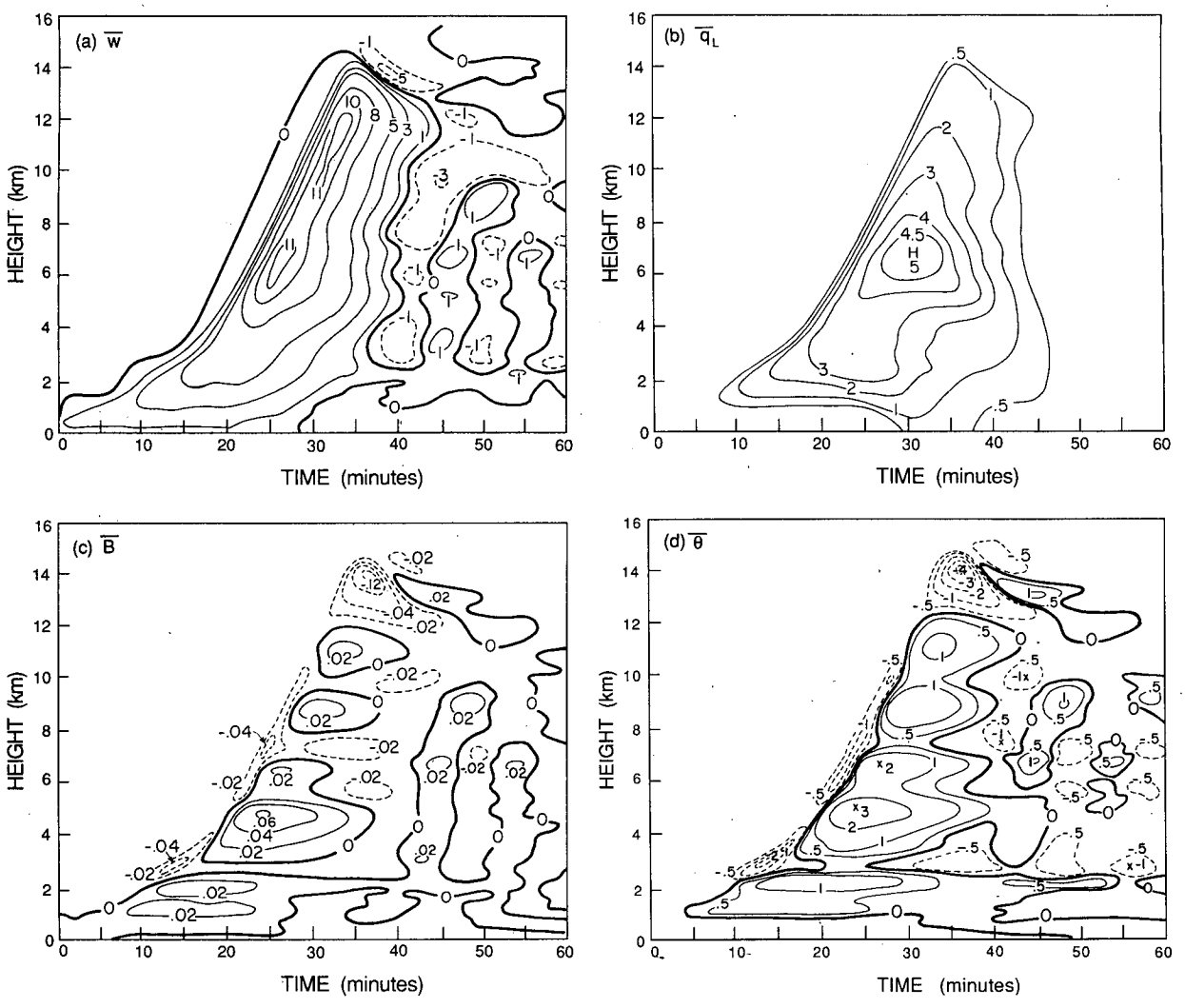

FIG. 16. Time-height plots for run VI of (a) $\bar{w}$ in m s^{-1}, (b) $\overline{q_L}$ in g kg^{-1}, (c) $\bar{B}$ in m s^{-2}, and (d) $\bar{\theta}$ in °C.

the tropical tropopause. However, it is possible that convection of that intensity may have occurred during GATE but was not sampled by any of the aircraft.

By including the lateral eddy mixing scheme of (18) into the physics of the model, the convection that developed in run VIII was diminished significantly as air from the outer environment was rapidly mixed into the cell. From our experience, deep GATE clouds cannot be simulated if lateral turbulent mixing is incorporated into the physics of 1DTD cloud models.

Runs IX–XII test the sensitivity of the model convection to variations in the strength and duration of the gust-front-type forcing sustained at low levels. As Table 4 shows, the intensity of the convection was particularly sensitive to the magnitude of the low-level forcing, as it affects the total mass flux through cloud base, while the duration of the forcing was also important in cloud development by continually transporting warm, moist air up through cloud base. These runs point out the importance of using observations in real clouds to represent, carefully and judiciously, the mechanisms by which convection is initiated in cloud models.

6. Conclusions

A 1DTD cumulus model has been designed that eliminates much of the inconsistency among cloud-top height, vertical velocity, and water content that has characterized previous 1DTD cloud models. Deep cumulonimbus typical of the GATE region have been simulated and found to be consistent with vertical velocities sampled by aircraft, reflectivities observed by radar, and simulations by three-dimensional models of GATE convective cells.

Realistic deep-cloud simulations were obtained when

- An overturning thermal cap, similar to those observed in real clouds and simulated in higher-dimensional models, was included in the model and allowed to affect vertical mixing in the convective core.

- The lower section of the cell was allowed to taper inward with height, as suggested by GATE aircraft data. This shape made the dilution of the core by lateral entrainment less and allowed the convective cell to grow to realistic heights.
- Sustained forcing was applied in the boundary layer that parameterized the effects of lifting by tropical, oceanic gust fronts, which constituted the primary mechanism for triggering GATE convection.
- Perturbation pressure was made internally consistent with the horizontal distribution of vertical velocity in the thermal cap and in the lower part of the convective core.

It was also found that additional cell growth was obtained if the updraft was tilted, as was often observed in GATE—especially for the deepest cells observed in squall lines (Houze 1977). The slope simply allowed rain to fall out of the updraft and thus reduced water loading. In another experiment, lateral entrainment effects were set to zero, and the model updraft was more intense than any observed by GATE aircraft, suggesting that all deep GATE cumulonimbus are characterized by some lateral entrainment. However, it is possible that the most intense updrafts were not sampled by the aircraft.

The internally consistent model that we have designed and tested in this study could be used in a wide variety of applications. In a companion paper, ice-phase microphysics will be added to the model to diagnose the vertical distributions of hydrometeors, microphysical processes, and vertical structure of the updrafts for convective cells embedded in a midlatitude squall line.

Acknowledgments. The cooperation of Drs. Joanne Simpson and Michael McCumber in providing information on three-dimensional model results are greatly appreciated. The figures were skillfully drafted by Mrs. Kay Y. Dewar. This research was supported by the National Science Foundation under Grants ATM8413546 and ATM8719838 and computing was provided by the National Center for Atmospheric Research.

APPENDIX A

Microphysical Parameterization

1. Condensation and evaporation of cloud water (PCOND)

Following Yau and Austin (1979), the rate of condensation of water vapor to cloud water is

$$\text{PCOND} = \rho_e(\overline{q_{vc}} - q_{vs})/\Delta t\left(1 + \frac{L^2 q_{vs}}{C_p R_v T_c^2}\right), \quad \text{(A1)}$$

where Δt is the model time step, $\overline{q_{vc}}$ the water vapor mixing ratio in the cell, q_{vs} the saturation mixing ratio with respect to water, T_c the cell temperature, L the latent heat of vaporization, C_p the specific heat of air at constant pressure, and R_v the gas constant for water vapor. Cloud water condenses if $\overline{q_{vc}} > q_{vs}$ and evaporates if $\overline{q_{vc}} < q_{vs}$.

2. Autoconversion of cloud water into rain (PRAUT)

The collision and coalescence of cloud droplets to form raindrops is parameterized following Kessler (1969) as

$$\text{PRAUT} = \rho_e \alpha \max[0., (\overline{q_{cw}} - q_{c0})] \quad \text{(A2)}$$

with $\alpha = 0.001\ \text{s}^{-1}$ and $q_{c0} = 1.0\ \text{g kg}^{-1}$.

3. The collection of cloud water by rain (PRACW)

The growth of raindrops through the collection of cloud droplets is assumed to follow the continuous collection equation, where

$$\frac{dM_r}{dt}(D_r) = \frac{\pi}{4}\rho_e \overline{q_{cw}} E_{rc} D_r^2 V_r(D_r), \quad \text{(A3)}$$

D_r is the diameter of the raindrops, and E_{rc} is the collection efficiency of cloud droplets by falling raindrops (assumed to be unity). The raindrops are assumed to have an inverse exponential size distribution given by

$$N(D_r) = N_{0r} \exp(-\lambda_r D_r), \quad \text{(A4)}$$

where N_{0r} is $8 \times 10^6\ \text{m}^{-4}$ (Marshall and Palmer 1948),

$$\lambda_r = \left(\frac{\pi \rho_L N_{0r}}{\rho_e \overline{q_r}}\right)^{1/4} \quad \text{(A5)}$$

and ρ_L is the density of liquid water. Multiplying (A3) by (A4) and integrating over all drop sizes yields

$$\text{PRACW} = \frac{\pi}{4}\Gamma(3 + b_r)\rho_e \overline{q_{cw}} N_{0r}\left(\frac{p_0}{p_c}\right)^{0.4} a_r \lambda_r^{-(3+b_r)} \quad \text{(A6)}$$

(see section 2e for values of parameters).

4. Evaporation of rain (PREVP)

The evaporation of rain is calculated following Rutledge and Hobbs (1983):

$$\text{PREVP} = 2\pi(S - 1)N_{0r}B^{-1} \times \left[\frac{0.78}{\lambda_r^2} + 0.31\text{Sc}^{1/3}\Gamma(2.5 + 0.5b_r)\left(\frac{\rho_e a_r}{\mu}\right)^{1/2} \times \left(\frac{p_0}{p_c}\right)^{0.2} \lambda_r^{-(2.5+0.5b_r)}\right], \quad \text{(A7)}$$

where $S = \overline{q_{vc}}/q_{vs}$, μ is the dynamic viscosity of air, Sc is the Schmidt number,

$$B = \frac{L_v}{K_a T_c}\left(\frac{L_v}{R_v T_c} - 1\right) + \frac{1}{\rho_e q_{vs} \phi}, \quad \text{(A8)}$$

K_a is the thermal conductivity of air, and ϕ is the diffusivity of water vapor in air.

APPENDIX B

Derivation of the Pressure Perturbation Equation

To derive the pressure perturbation equation, the accelerations in the radial flow must be known throughout the interior of the convective core. This is found by substituting (42) into (6), which, after some manipulation, becomes

$$\frac{du(r)}{dt} = r^3\left[\frac{5}{9}\frac{\Lambda_1^2}{\rho_e^2} - \frac{1}{3\rho_e}\frac{\partial}{\partial z}\left(\frac{w_0 x \Lambda_1}{R}\right)\right] + r^2\left\{\frac{1}{3\rho_e}\frac{\partial}{\partial z}\left[\frac{\rho_e}{R}\frac{\partial(w_0 x)}{\partial t}\right] + \frac{1}{\rho_e} \times \frac{\partial}{\partial z}\left(\frac{w_0\Lambda_1}{3} + \frac{w_0 x \Lambda_2}{2R}\right) - \frac{4}{3}\frac{\Lambda_1\Lambda_2}{\rho_e^2}\right\} + r\left[\frac{3}{4}\frac{\Lambda_2^2}{\rho_e^2} - \frac{1}{2\rho_e}\frac{\partial}{\partial z}\left(\rho_e\frac{\partial w_0}{\partial t} + w_0\Lambda_2\right)\right], \quad \text{(B1)}$$

where

$$\Lambda_1 = \frac{\partial}{\partial z}\left(\frac{\rho_e w_0 x}{R}\right) \quad \text{and} \quad \Lambda_2 = \frac{\partial(\rho_e w_0)}{\partial z}. \quad \text{(B2)}$$

By separating the dependence of r in each of the terms (B1) and substituting into (42), the resulting perturbation pressure equation is

$$\tilde{p} = \tilde{p} + \frac{R^4}{6}\left[\frac{5}{9}\frac{\Lambda_1^2}{\rho_e} - \frac{1}{3}\frac{\partial}{\partial z}\left(\frac{w_0 x \Lambda_1}{R}\right)\right] + \frac{R^3}{5}\left\{\frac{1}{3}\frac{\partial}{\partial z}\left[\frac{\rho_e}{R}\frac{\partial(w_0 x)}{\partial t}\right] \times \frac{\partial}{\partial z}\left(\frac{w_0\Lambda_1}{3} + \frac{w_0 x\Lambda_2}{2R}\right) - \frac{4}{3}\frac{\Lambda_1\Lambda_2}{\rho_e}\right\} + \frac{R^2}{4}\left[\frac{3}{4}\frac{\Lambda_2^2}{p_e^2} - \frac{1}{2}\frac{\partial}{\partial z}\left(p_e\frac{\partial w_0}{\partial t} + w_0\Lambda_2\right)\right]. \quad \text{(B3)}$$

After rearranging (B3), dividing by R^2, and making further mathematical manipulations with the aid of (24):

$$\left[\frac{8x-15}{40(3-2x)}\right]\frac{\partial}{\partial z}\left(\rho_e\frac{\partial\bar{w}}{\partial t}\right) + \left\{\frac{R}{5}\frac{\partial}{\partial z}\left[\frac{x}{(3-2x)R}\right] - \frac{3}{8}\frac{\partial}{\partial z}\left(\frac{1}{3-2x}\right)\right\} \times \left(\rho_e\frac{\partial\bar{w}}{\partial t}\right) + \frac{1}{R^2}(\tilde{p}-\bar{p}) = \Lambda_3, \quad \text{(B4)}$$

$$\Lambda_3 = -\frac{5R^2\Lambda_1^2}{54\rho_e} + \frac{4R\Lambda_1\Lambda_2}{15\rho_e} - \frac{3\Lambda_2^2}{16\rho_e} + \frac{R^2}{18}\frac{\partial}{\partial z}\left(\frac{w_0 x\Lambda_1}{R}\right) - \frac{R}{5}\frac{\partial}{\partial z}\left(\frac{w_0\Lambda_1}{3} + \frac{w_0 x\Lambda_2}{2R}\right) + \frac{1}{8}\frac{\partial}{\partial z}(w_0\Lambda_2) + \frac{3}{8}\frac{\partial}{\partial z}\left[\rho_e\bar{w}\frac{\partial}{\partial t}\left(\frac{1}{3-2x}\right)\right] - \frac{R}{5}\frac{\partial}{\partial z}\left[\frac{\rho_e\bar{w}}{R}\frac{\partial}{\partial t}\left(\frac{x}{3-2x}\right)\right]. \quad \text{(B5)}$$

Rearranging the vertical momentum equation given by (8) and (9), substituting into (B4), and using (15) to represent p in terms of the nondimensional pressure P, the final form of the perturbation pressure equation is

$$\left[\frac{15-8x}{40(3-2x)}\right](R_d\rho_e\theta_{ve})\frac{\partial^2\bar{P}}{\partial z^2} + \left\langle R_d\rho_e\theta_{ve}\left\{\frac{3}{8}\frac{\partial}{\partial z}\left(\frac{1}{3-2x}\right) - \frac{R}{5}\frac{\partial}{\partial z}\left[\frac{x}{(3-2x)R}\right]\right\} + \left[\frac{15-8x}{40(3-2x)}\right]\frac{\partial}{\partial z}(R_d\rho_e\theta_{ve})\right\rangle \times \frac{\partial\bar{P}}{\partial z} + \frac{R_d\rho_e\theta_{ve}}{R^2}(\tilde{p}-\bar{p}) = \Lambda_4, \quad \text{(B6)}$$

$$\Lambda_4 = \Lambda_3 + \left[\frac{15-8x}{40(3-2x)}\right]\frac{\partial}{\partial z}\left[\rho_e\bar{B} + \rho_e\left(\frac{\partial\bar{w}}{\partial t}\right)_{\text{adv}}\right] + \left\{\frac{3}{8}\frac{\partial}{\partial z}\left(\frac{1}{3-2x}\right) - \frac{R}{5}\frac{\partial}{\partial z}\left[\frac{x}{(3-2x)R}\right]\right\} \times \rho_e\left[\bar{B} + \left(\frac{\partial\bar{w}}{\partial t}\right)_{\text{adv}}\right], \quad \text{(B7)}$$

where $(\partial w/\partial t)_{\text{adv}}$ is given by terms (ii)–(iv) in (8). Because it is a one-dimensional elliptic equation for $\bar{P}$, (A6) can be solved using the method of Richtmyer and Morton (1967) and the boundary conditions given by (44) and (45).

REFERENCES

Addis, R. P., M. Garstang and G. D. Emmitt, 1984: Downdrafts from tropical oceanic cumuli. *Bound.-Layer Meteor.*, **28**, 23–49.

Adler, R. F., and R. A. Mack, 1984: Thunderstorm height–rainfall rate relations for use with satellite rainfall estimation techniques. *J. Climate Appl. Meteor.*, **23**, 280–296.

——, and ——, 1986: Thunderstorm cloud top dynamics as inferred from satellite observations and a cloud top parcel model. *J. Atmos. Sci.*, **43**, 1945–1960.

——, and A. J. Negri, 1988: A satellite infrared technique to estimate tropical convective and stratiform rainfall. *J. Climate Appl. Meteor.*, in press.

Anthes, R. A., 1977: A cumulus parameterization scheme utilizing a one-dimensional cloud model. *Mon. Wea. Rev.*, **105**, 270–286.

Arakawa, A., and W. Schubert, 1974: Interaction of a cumulus cloud ensemble with the large-scale environment. Part I. *J. Atmos. Sci.*, **35**, 674–701.

Asai, T., and A. Kasahara, 1967: A theoretical study of the compensating downward motions associated with cumulus clouds. *J. Atmos. Sci.*, **24**, 487–496.

Austin, P. H., M. B. Baker, A. M. Blyth and J. B. Jensen, 1985: Small-scale variability in warm continental cumulus clouds. *J. Atmos. Sci.*, **42**, 1123–1138.

Boatman, J. F., and A. H. Auer, Jr., 1983: The role of cloud top entrainment in cumulus clouds. *J. Atmos. Sci.*, **40,** 1517–1534.

Brown, J. M., 1979: Mesoscale unsaturated downdrafts driven by rainfall evaporation. A numerical study. *J. Atmos. Sci.*, **36,** 313–338.

Chong, M., P. Amayenc, G. Scialom and J. Testud, 1987: A tropical squall line observed during the COPT 81 experiment in Africa. Part I: Kinematic structure inferred from dual-Doppler radar data. *Mon. Wea. Rev.*, **115,** 670–694.

Cotton, W. R., 1975: On parameterization of turbulent transport in cumulus clouds. *J. Atmos. Sci.*, **32,** 548–564.

——, and G. Tripoli, 1978: Cumulus convection in shear flow—three-dimensional numerical experiments. *J. Atmos. Sci.*, **35,** 1503–1531.

Crowley, W. P., 1968: Numerical advection experiments. *Mon. Wea. Rev.*, **96,** 1–11.

Dudhia, J., M. W. Moncrieff and D. K. W. So, 1987: The two-dimensional dynamics of West African squall lines. *Quart. J. Roy. Meteor. Soc.*, **113,** 121–146.

Emmitt, G. D., 1978: Tropical cumulus interaction with and modification of the subcloud region. *J. Atmos. Sci.*, **35,** 1485–1502.

Foote, G. B., and P. S. DuToit, 1969: Terminal velocity of raindrops aloft. *J. Appl. Meteor.*, **8,** 249–253.

Frank, W. M., 1978: The life cycles of GATE convective systems. *J. Atmos. Sci.*, **35,** 1256–1264.

——, and C. Cohen, 1987: Simulation of tropical convective systems. Part I: A cumulus parameterization. *J. Atmos. Sci.*, **44,** 3787–3799.

——, G. D. Emmitt and C. Warner, 1981: Multiscale analysis of low-level vertical fluxes on day 261 of GATE. *J. Atmos. Sci.*, **38,** 1964–1976.

Fritsch, J. M., and C. G. Chappell, 1980: Numerical prediction of convectively driven mesoscale pressure systems. Part II. Mesoscale model. *J. Atmos. Sci.*, **37,** 1734–1762.

Gamache, J. F., and R. A. Houze, Jr., 1982: Mesoscale air motions associated with a tropical squall line. *Mon. Wea. Rev.*, **110,** 118–135.

——, and ——, 1983: Water budget of a mesoscale convective system in the tropics. *J. Atmos. Sci.*, **40,** 1835–1850.

——, and ——, 1985: Further analysis of the composite wind and thermodynamic structure of the 12 September GATE squall line. *Mon. Wea. Rev.*, **113,** 1241–1259.

Griffith, C. G., J. A. Augustine and W. L. Woodley, 1981: Satellite rain estimation in the U.S. High Plains. *J. Appl. Meteor.*, **20,** 53–66.

Hallett, J., R. I. Sax, D. Lamp and A. S. R. Murty, 1978: Aircraft measurements of ice in Florida cumuli. *Quart. J. Roy. Meteor. Soc.*, **104,** 631–651.

Hildebrand, F. B., 1976: *Advanced Calculus for Applications.* Prentice Hall, 733 pp.

Holton, J. R., 1973: A one-dimensional cumulus model including pressure perturbations. *Mon. Wea. Rev.*, **101,** 201–205.

Houze, R. A., Jr., 1977: Structure and dynamics of a tropical squall-line system. *Mon. Wea. Rev.*, **105,** 1540–1567.

——, and A. K. Betts, 1981: Convection in GATE. *Rev. Geophys. Space Phys.*, **19,** 541–576.

——, and E. N. Rappaport, 1984: Air motions and precipitation structure of an early summer squall line over the eastern tropical Atlantic. *J. Atmos. Sci.*, **41,** 553–574.

——, C.-P. Cheng, C. A. Leary and J. F. Gamache, 1980: Diagnosis of cloud mass and heat fluxes from radar and synoptic data. *J. Atmos. Sci.*, **37,** 754–773.

Jensen, J. B., P. M. Austin, M. B. Baker and A. M. Blyth, 1985: Turbulent mixing, spectral evolution and dynamics in a warm cumulus cloud. *J. Atmos. Sci.*, **42,** 173–192.

Johnson, R. H., 1978: Cumulus transports in a tropical wave composite for Phase III of GATE. *J. Atmos. Sci.*, **35,** 484–494.

——, 1980: Diagnosis of convective and mesoscale motions during Phase III of GATE. *J. Atmos. Sci.*, **37,** 733–753.

Jorgensen, D. P., E. J. Zipser and M. A. LeMone, 1985: Vertical motions in intense hurricanes. *J. Atmos. Sci.*, **42,** 839–856.

Kessler, E., 1969: *On the Distribution and Continuity of Water Substance in Atmospheric Circulations. Meteor. Monogr.*, No. 32, Amer. Meteor. Soc., 84 pp.

Kreitzberg, C. W., and D. J. Perkey, 1977: Release of potential instability. Part II. The mechanism of convective/mesoscale interactions. *J. Atmos. Sci.*, **34,** 1569–1595.

Kyle, T. G., W. R. Sand and D. J. Musil, 1976: Fitting measurements of thunderstorm updraft profiles to model profiles. *Mon. Wea. Rev.*, **104,** 611–617.

LaMontagne, R. G., and J. W. Telford, 1983: Cloud top mixing in small cumuli. *J. Atmos. Sci.*, **40,** 2148–2156.

Leary, C. A., and R. A. Houze, Jr., 1979: Melting and evaporation of hydrometeors in precipitation from the anvil clouds of deep tropical convection. *J. Atmos. Sci.*, **36,** 669–679.

LeMone, M. A., G. M. Barnes, E. J. Szoke and E. J. Zipser, 1984: The tilt of the leading edge of mesoscale tropical convective lines. *Mon. Wea. Rev.*, **112,** 510–519.

——, and E. J. Zipser, 1980: Cumulonimbus vertical velocity events in GATE. Part I: Diameter, intensity, and mass flux. *Mon. Wea. Rev.*, **112,** 2444–2457.

Libersky, L. D., 1980: Turbulence in cumulus clouds. *J. Atmos. Sci.*, **37,** 2332–2346.

Lin, Y.-L., R. D. Farley and H. D. Orville, 1983: Bulk parameterization of the snow field in a cloud model. *J. Climate Appl. Meteor.*, **22,** 1065–1092.

Lopez, R. E., 1973: A parametric model of cumulus convection. *J. Atmos. Sci.*, **30,** 1354–1373.

McCarthy, J., 1974: Field verification of the relationship between entrainment rate and cumulus cloud diameter. *J. Atmos. Sci.*, **31,** 1028–1039.

Malkus, J. S., 1954: Some results of a trade-cumulus cloud investigation. *J. Meteor.*, **11,** 220–237.

——, and R. S. Scorer, 1955: The erosion of cumulus towers. *J. Meteor.*, **12,** 43–57.

Marshall, J. S., and W. M. Palmer, 1948: The distribution of raindrops with size. *J. Meteor.*, **5,** 165–166.

Murray, F. W., 1970: Numerical models of a tropical cumulus cloud with bilateral and axial symmetry. *Mon. Wea. Rev.*, **98,** 14–28.

——, 1971: Humidity augmentation as an initial impulse in a numerical cloud model. *Mon. Wea. Rev.*, **99,** 37–48.

——, and L. R. Koenig, 1972: Numerical experiments on the relations between microphysics and dynamics in cumulus convection. *Mon. Wea. Rev.*, **100,** 717–732.

Nicholls, M. E., 1987: A comparison of the results of a two-dimensional numerical simulation of a tropical squall line with observations. *Mon. Wea. Rev.*, **115,** 3055–3077.

Nitta, T., 1977: Response of cumulus updraft and downdraft to GATE A/B-scale motion systems. *J. Atmos. Sci.*, **34,** 1163–1186.

Ogura, Y., and H.-R. Cho, 1973: Diagnostic determination of cumulus cloud populations from observed large-scale variables. *J. Atmos. Sci.*, **30,** 1276–1286.

——, and M.-T. Liou, 1980: The structure of a midlatitude squall line: A case study. *J. Atmos. Sci.*, **37,** 553–567.

——, and T. Takahashi, 1971: Numerical simulation of the life cycle of a thunderstorm cell. *Mon. Wea. Rev.*, **99,** 895–911.

Paluch, I. R., 1979: The entrainment mechanism in Colorado cumuli. *J. Atmos. Sci.*, **36,** 2467–2478.

Pointin, Y., 1985: Numerical simulation of organized convection. Part I: Model description and preliminary comparisons with squall line observations. *J. Atmos. Sci.*, **42,** 155–172.

Randall, D. A., and G. J. Huffman, 1982: Entrainment and detrainment in a simple cumulus cloud. *J. Atmos. Sci.*, **39,** 2793–2806.

Raymond, D. J., 1979: A two-scale model of moist, nonprecipitating convection. *J. Atmos. Sci.*, **36,** 816–831.

Richtmyer, R. D., and K. W. Morton, 1967: *Difference Methods for Initial-Value Problems.* Interscience Publishers, 405 pp.

Rotunno, R., J. B. Klemp and W. L. Weisman, 1988: A theory for strong, long-lived squall lines. *J. Atmos. Sci.*, **45,** 463–485.

Roux, F., 1985: The retrieval of thermodynamic fields from multiple-Doppler radar data using the equation of motion and the thermodynamic equation. *Mon. Wea. Rev.*, **113,** 219–235.

——, J. Testud, M. Payen and B. Pinty, 1984: West African squall-line thermodynamic structure retrieved from dual-Doppler radar observations. *J. Atmos. Sci.*, **41**, 3104–3121.

Rutledge, S. A., and P. V. Hobbs, 1984: The mesoscale and microscale structure and organization of clouds and precipitation in mid-latitude cyclones. XII: A diagnostic modeling study of precipitation development in narrow cold-frontal rainbands. *J. Atmos. Sci.*, **41**, 2949–2972.

——, and R. A. Houze, 1987: A diagnostic modeling study of the trailing stratiform region of a midlatitude squall line. *J. Atmos. Sci.*, **44**, 2640–2656.

Ryan, B. F., and P. Lalousis, 1979: A one-dimensional time-dependent model for cumulus. *Quart. J. Roy. Meteor. Soc.*, **105**, 615–628.

Sand, W. R., 1976: Observations in hailstorms using the T-28 aircraft system. *J. Appl. Meteor.*, **15**, 641–650.

Saunders, P. M., 1962: Penetrative convection in stably stratified fluids. *Tellus*, **14**, 177–194.

Schlesinger, R. E., 1978a: A three-dimensional model of an isolated thunderstorm. Part I. Comparative experiments for variable ambient wind shear. *J. Atmos. Sci.*, **35**, 690–713.

——, 1978b: Nonlinear eddy-viscosity turbulence parameterization in anelastic three-dimensional flow. Some mathematical aspects. *J. Atmos. Sci.*, **35**, 2268–2273.

Scorer, R. S., 1957: Experiments on convection of isolated masses of buoyant fluid. *J. Fluid Mech.*, **2**, 583–594.

——, and F. H. Ludlam, 1953: Bubble theory of convection. *Quart. J. Roy Meteor. Soc.*, **79**, 94–103.

——, and C. Ronne, 1956: Experiments with convection bubbles. *Weather*, **11**, 151–154.

Simpson, J., 1980: Downdrafts as linkages in dynamic cumulus seeding effects. *J. Appl. Meteor.*, **19**, 477–487.

——, 1983a: Cumulus clouds hypothesis: Early aircraft observations and entrainment hypothesis. *Mesoscale Meteorology—Theories, Observations and Models*, D. K. Lilly and T. Gal-Chen, Eds., Reidel, 355–373.

——, 1983b: Cumulus clouds: Interactions between laboratory experiments and observations as foundations for models. *Mesoscale Meteorology—Theories, Observations and Models*, D. K. Lilly and T. Gal-Chen, Eds., Reidel, 399–412.

——, 1983c: Cumulus clouds: Numerical models, observations and entrainment. *Mesoscale Meteorology—Theories, Observations and Models*, D. K. Lilly and T. Gal-Chen, Eds., Reidel, 413–445.

——, and V. Wiggert, 1969: Models of precipitating cumulus towers. *Mon. Wea. Rev.*, **97**, 471–489.

——, and G. van Helvoirt, 1980: GATE cloud–subcloud interactions examined using a three-dimensional cumulus model. *Contrib. Atmos. Phys.*, **53**, 106–134.

——, —— and M. McCumber, 1982: Three-dimensional simulations of cumulus congestus clouds on GATE day 261. *J. Atmos. Sci.*, **39**, 126–145.

——, B. R. Morton, M. C. McCumber and R. S. Penc, 1986: Observations and mechanisms of GATE waterspouts. *J. Atmos. Sci.*, **43**, 753–782.

Smull, B. F., and R. A. Houze, Jr., 1985: A midlatitude squall line with a trailing region of stratiform rain: Radar and satellite observations. *Mon. Wea. Rev.*, **113**, 117–133.

——, and ——, 1987a: Dual-Doppler radar analysis of a midlatitude squall line with a trailing region of stratiform rain. *J. Atmos. Sci.*, **44**, 2128–2148.

——, and ——, 1987b: Rear inflow in squall lines with trailing stratiform precipitation. *Mon. Wea. Rev.*, **115**, 2869–2889.

Soong, S.-T., and Y. Ogura, 1973: A comparison between axisymmetric and slab-symmetric cumulus cloud models. *J. Atmos. Sci.*, **30**, 879–893.

——, and ——, 1976: A determination of the trade-wind cumuli population using BOMEX data and an axisymmetric cloud model. *J. Atmos. Sci.*, **33**, 992–1007.

Squires, P., 1958: Penetrative downdraughts in cumuli. *Tellus*, **10**, 381–389.

Srivastava, R. C., 1985: A simple model of evaporatively driven downdraft: Application to microburst downdraft. *J. Atmos. Sci.*, **42**, 1004–1023.

——, 1987: A model of intense downdrafts driven by the melting and evaporation of precipitation. *J. Atmos. Sci.*, **44**, 1752–1773.

——, T. J. Matejka and T. J. Lorello, 1986: Doppler radar study of the trailing anvil region associated with a squall line. *J. Atmos. Sci.*, **43**, 356–377.

Szoke, E. J., and E. J. Zipser, 1986: A radar study of convective cells in mesoscale systems in GATE. Part II: Life cycles of convective cells. *J. Atmos. Sci.*, **43**, 199–218.

——, —— and D. P. Jorgensen, 1986: A radar study of convective cells in mesoscale systems in GATE. Part I: Vertical profile statistics and comparison with hurricanes. *J. Atmos. Sci.*, **43**, 182–197.

Tao, W.-K., and J. Simpson, 1984: Cloud interactions and merging numerical simulations. *J. Atmos. Sci.*, **41**, 2901–2917.

——, and S.-T. Soong, 1986: A study of the response of deep tropical clouds to mesoscale processes. Three-dimensional numerical experiments. *J. Atmos. Sci.*, **43**, 2653–2676.

Telford, J. W., and P. B. Wagner, 1981: Observations of condensate growth determined by entity type mixing. *Pure Appl. Geophys.*, **119**, 934–965.

Tripoli, G. J., and W. R. Cotton, 1980: A numerical investigation of several factors contributing to the observed variable intensity of deep convection over south Florida. *J. Appl. Meteor.*, **19**, 1037–1063.

Turner, J. S., 1962: The starting plume in neutral surroundings. *J. Fluid Mech.*, **13**, 356–368.

Turpeinen, O., and M. K. Yau, 1981: Comparison of results from a three-dimensional cloud model with statistics of radar echoes on day 261 of GATE. *Mon. Wea. Rev.*, **109**, 1495–1511.

van Helvoirt, G., 1980: Three-dimensional simulations of the effects of ambient wind shear on convective clouds of the GATE on day 261. M.S. thesis, Univ. of Virginia, 108 pp.

Warner, C., and G. L. Austin, 1978: Statistics of radar echoes on day 261 of GATE. *Mon. Wea. Rev.*, **106**, 983–994.

——, J. Simpson, D. W. Martin, D. Suchman, F. R. Mosher and R. F. Reinking, 1979: Shallow convection on day 261 of GATE. Mesoscale area. *Mon. Wea. Rev.*, **107**, 1617–1635.

——, ——, G. van Helvoirt, D. W. Martin, D. Suchman and G. L. Austin, 1980: Deep convection on day 261 of GATE. *Mon. Wea. Rev.*, **108**, 169–194.

Warner, J., 1969: The microstructure of cumulus cloud. Part I. General features of the droplet spectrum. *J. Atmos. Sci.*, **26**, 1049–1059.

——, 1970: On steady-state one-dimensional models of cumulus convection. *J. Atmos. Sci.*, **27**, 1035–1040.

Woodward, B., 1959: The motion in and around an isolated thermal. *Quart. J. Roy. Meteor. Soc.*, **85**, 144–151.

Wylie, D. P., 1979: An application of a geostationary satellite rain estimation technique to an extratropical area. *J. Appl. Meteor.*, **18**, 1640–1648.

Yanai, M., S. Esbensen and J. H. Chu, 1973: Determination of bulk properties of tropical cloud clusters from large-scale heat and moisture budgets. *J. Atmos. Sci.*, **30**, 611–627.

Yau, M. K., 1979: Perturbation pressure and cumulus convection. *J. Atmos. Sci.*, **36**, 690–694.

——, 1980: The effect of evaporation, water load and wind shear on cloud development in a three-dimensional numerical model. *J. Atmos. Sci.*, **37**, 488–494.

——, and P. M. Austin, 1979: A model for hydrometeor growth and evolution of raindrop size spectra in cumulus cells. *J. Atmos. Sci.*, **36**, 655–668.

Zipser, E. J., 1977: Mesoscale and convective-scale downdrafts as distinct components of squall-line circulation. *Mon. Wea. Rev.*, **105**, 1568–1589.

——, and M. A. LeMone, 1980: Cumulonimbus vertical velocity events in GATE. Part II: Synthesis and model core structure. *J. Atmos. Sci.*, **37**, 2458–2469.